Rain retrieval from dual-frequency radar Doppler spectra: validation and potential for a midlatitude precipitating case-study

RMetS
Royal Meteorological Society

Rain retrieval from dual-frequency radar Doppler spectra: validation and potential for a midlatitude precipitating case-study

F. Tridon,[a]* A. Battaglia,[a,b] E. Luke[c] and P. Kollias[d]

[a]*Department of Physics and Astronomy, University of Leicester, UK*
[b]*NERC, National Center for Earth Observation, University of Leicester, UK*
[c]*Atmospheric Sciences Division, Brookhaven National Laboratory, Upton, NY, USA*
[d]*School of Marine and Atmospheric Sciences, Stony Brook University, NY, USA*

*Correspondence to: F. Tridon, Space Research Center, Department of Physics and Astronomy, Michael Atiyah Building, University of Leicester, University Road, Leicester LE1 7RH, UK. E-mail: f.tridon@leicester.ac.uk

A recently developed technique retrieving the binned raindrop size distributions (DSDs) and air state parameters from ground-based K_a and W-band radars Doppler spectra profiles is improved and applied to a typical midlatitude rain event. The retrievals are thoroughly validated against DSD observations of a 2D video disdrometer and independent X-band observations. For this case-study, profiles of rain rate, R, mean volume diameter and concentration parameter are retrieved, with low bias and standard deviations. In light rain ($0.1 < R < 1\,\mathrm{mm\,h^{-1}}$), the radar reflectivities must be calibrated with a collocated disdrometer which introduces random errors due to sampling mismatch between the two instruments. The best performances are obtained in moderate rain ($1 < R < 20\,\mathrm{mm\,h^{-1}}$) where the retrieval is providing self-consistent estimates of the absolute calibration and of the attenuation caused by antenna or radome wetness for both radars.

Key Words: drop size distribution; rain microphysics; midlatitude precipitation; dual-wavelength radar

Received 10 June 2016; Revised 21 December 2016; Accepted 23 January 2017; Published online in Wiley Online Library 11 April 2017

1. Introduction

Accurate measurements of drop size distribution (DSD) profiles are crucial for understanding the processes governing cloud and precipitation microphysics, which are of primary importance in correctly simulating the state of the atmosphere. In fact, microphysical processes – such as condensation of water vapour, collision and coalescence between the droplets, evaporation in unsaturated air, and droplet break-up – are obviously critical in shaping the properties of the rain falling at the ground, like rainfall rate (R) or mean drop diameter. But, in addition, through latent heating/cooling, they can directly influence the thermodynamics of precipitation systems and affect their evolution. For example, rain evaporation plays an important role in creating downdraughts under the cloud base (Li and Srivastava, 2001) with its efficiency heavily depending on the DSD. Similarly, changing the threshold diameter at which break-up occurs significantly affects the mean precipitation rate in large-scale precipitation systems (Morrison *et al.*, 2012).

Current models mostly use bulk microphysics schemes with one or two prognostic variables and parametrized particle size distribution. Two-moment bulk microphysics schemes predicting both mixing ratio and number concentration have become increasingly popular over the last decade because of their flexibility in parametrizing processes like break-up, which affects the number concentration but not the mixing ratio. Several cloud-resolving model studies have pointed out the critical need for observations capable of validating the additional prognostic variables of the models (Morrison and Milbrandt, 2011). In particular, Morrison *et al.* (2012) found significant discrepancies in the DSD properties (mean diameter, concentration and shape) at the ground between simulation and disdrometer observations of a squall line and highlighted the lack of observations of the DSD aloft.

Routine measurements of profiles of precipitation microphysics are realistically only possible with remote-sensing observations and require sophisticated retrieval techniques. A large number of these techniques using ground-based radars have been proposed in the past. Polarimetric radar techniques derive the bulk properties of the DSD (characteristic size and width, concentration parameter and rain rate) by exploiting the difference in the reflectivity, Doppler velocity and propagation at vertical and horizontal polarization, which is particularly pronounced at low elevation angles and for large raindrops (Wilson *et al.*, 1997; Bringi *et al.*, 2009, and references therein). Similarly, thanks to the unambiguous relationship between raindrop fall speeds and sizes, vertically pointing Doppler radars can provide information on the DSD shape through the retrieval of parametrized or binned DSDs. For example, dual-frequency wind profiler methods have been used extensively over the last two decades and are known

to be accurate in steady stratiform rain (Cifelli *et al.*, 2000; Gage *et al.*, 2002; Williams, 2016, and references therein). They are limited, however, by the low sensitivity and large beam width of wind profilers, which leads to coarse time and range resolutions and to increased errors in strong convective rain because of turbulence and wind shear (Schafer *et al.*, 2002). Other techniques make use of non-Rayleigh scattering signatures observed in the Doppler spectra of vertically pointing cloud radars (Kollias *et al.*, 2002; Giangrande *et al.*, 2012). They retrieve the size and shape parameters of the DSD at a very high temporal and range resolution. However, they cannot provide a concentration parameter, nor rain rate because of the strong attenuation of cloud radar signals in rain. Moreover, they are limited to moderate rainfall cases where large enough drops are present in order to produce significant non-Rayleigh scattering signatures, and where rain attenuation is not too important.

In this article the focus is on midlatitude precipitation which is dominated both by light ($0.1 < R < 1\,\mathrm{mm\,h^{-1}}$) and intermediate ($1 < R < 10\,\mathrm{mm\,h^{-1}}$) rainfall conditions. For instance, from two different sort of datasets, Mugnai *et al.* (2005) and Lin and Hou (2012) showed that these types of precipitation represent nearly 90% of the rain volume and 70% of the rain occurrence over Europe and over the Continental USA, respectively. For such regimes, a recently developed technique formulated in Tridon and Battaglia (2015) shows great potential for profiling the properties of the DSD at high resolution from the combination of observed radar Doppler spectra at K_a- and W-band. The technique consists of two successive steps. In Tridon and Battaglia (2015), the first step was extensively validated thanks to synthetic data. However the second step was only tested on a single profile in stratiform conditions. The reflectivity forwarded from the retrievals was compared with independent measurements of a collocated wind profiler and showed promising results. Yet, a thorough validation was not possible due to the lack of additional *in situ* observations. The retrieval main output, namely the DSD, still needs to be carefully validated and its consistency over time needs to be verified on continuous observations.

The retrieval of rain bulk properties from radar observations implies that measured reflectivity is absolutely calibrated. Radar calibration is a longstanding issue which seriously limits the accuracy of radar retrievals. In particular for cloud radars, the attenuation due to antenna or radome wetness during precipitation is an additional effect and cannot be easily distinguished from miscalibration (Hogan *et al.*, 2003). Since the Tridon and Battaglia (2015) retrieval second step used K_a–W differential attenuation, absolute calibration of the radars was not required but could have been derived *a posteriori* by comparing the measured reflectivities and retrieved DSDs. An important part of the current work is the complete redesign of the second step of the retrieval. In this new version, the calibration constants of the radars are parameters which are explicitly retrieved.

Because it combines the Doppler spectra observations from two collocated radars, the retrieval is particularly demanding, both in terms of observational and computational resources. Before being applied to an extensive dataset of several months, its potential for providing accurate rain microphysics observations needs to be established on a full rain event including, if possible, various rain characteristics. Until recent years, multi-frequency Doppler radar observations have been scarce but their interest is continuously growing. For example, the ongoing deployment of multi-frequency Doppler radar systems, in the framework of the US Department of Energy Atmospheric Research Measurement (ARM) program (Mather and Voyles, 2013), promises large amounts of dual-frequency Doppler observations in the near future, which will provide a unique dataset for evaluating and constraining microphysical simulations.

This article describes the application of the technique presented in Tridon and Battaglia (2015) for a case-study observed in summer 2014 during the Biogenic Aerosols Effects on Clouds and Climate (BAECC) field campaign in Finland, where collocated disdrometer and multi-frequency Doppler radar observations where both available. Section 2 describes the case-study while section 3 quickly summarizes the first step of the retrieval and fully describes the new version of the second step. Then, results and validation for this case-study are presented in sections 4 and 5, respectively. Finally, the absolute calibration of cloud radars provided by the retrieval is discussed in section 6 and conclusions are presented in section 7.

2. The 7 June 2014 rain event

This study focuses on a midlatitude stratiform precipitation event that occurred on 7 June 2014 at Hyytiälä in Finland during the BAECC field campaign (Petäjä *et al.*, 2016). The deployment of the ARM Mobile Facility contributed to an unprecedented suite of observations. In particular, the K_a-band ARM Zenith Radar (KAZR) and the Marine W-band ARM Cloud Radar (MWACR) were continuously measuring profiles of Doppler spectra, key inputs for the rain retrieval. A thorough validation of the retrieval is possible thanks to additional collocated instruments: a 2D video disdrometer (2DVD) (Kruger and Krajewski, 2002) that can be used as a ground-based reference for the DSD, and a third radar – the X-band Scanning ARM Cloud radar (X-SACR) – providing independent profile observations intermittently (i.e. only when it was operated in vertically pointing mode).

As with most midlatitude rain events, precipitation was initiated in the ice phase with a clear separation between low-reflecting ice crystals and fast-falling drops (see reflectivity and Doppler velocity panels in Figure 1) and a transitioning region at roughly 2.5 km corresponding to the freezing level. The ice clouds appear particularly jagged with cloud tops ranging between 4 and 8 km and a succession of several fall streaks. The initial phase of the event is quite intermittent with three light shallow showers between 1000 and 1100 UTC followed by some deeper and more continuous precipitation. Afterwards, moderate convection is triggered with some rapidly alternating updraughts and downdraughts visible in mean Doppler velocities around 1200 UTC. This convection induces some moderate rain causing the complete extinction of the W-band signal above 3 km. The corresponding rain rates ($\approx$16 $\mathrm{mm\,h^{-1}}$; Figure 2) are then close to the upper limit of applicability of this retrieval. From 1230 UTC, the precipitation then rapidly evolves into its stratiform type and slowly decays until it ends around 1500 UTC. Overall, the event lasted between 1010 and 1510 UTC with rain rates ranging between 0.01 $\mathrm{mm\,h^{-1}}$ (the lower limit of the 2DVD sensitivity) and 16 $\mathrm{mm\,h^{-1}}$ (Figure 2).

With a wide range of precipitation type and dynamic conditions (showers, stratiform, convection), this event epitomizes the character of precipitation in the mid to high latitudes where the modal rainfall rate is about 1 $\mathrm{mm\,h^{-1}}$ (Leinonen *et al.*, 2012) and is well suited to test the applicability of the K_a–W spectral methodology for light and intermediate rainfall rates.

The dual Doppler radar retrieval methodology is ideally suited to matched-beam radars. The KAZR and MWACR have slightly different beamwidths (0.33 and 0.36°, respectively) and pulse lengths (3.33 and 4 μs, respectively), and were operated few metres apart during BAECC. This latter drawback was addressed by applying a time shift of 6 s until matching was achieved for the mean Doppler velocities in Rayleigh target regions. Observations were then mapped onto a common time–height grid with resolution of 2 s and 30 m, as defined by the coarsest for the two radar sampling grids. The nearest Doppler spectra are selected for each point of the grid and interpolated on a common Doppler velocity vector, again using the observation with the coarsest resolution (in the configuration of BAECC, the Doppler velocities of both radars were almost perfectly matched with 2.37 and 2.35 $\mathrm{cm\,s^{-1}}$ Doppler resolution, respectively). Between 1000 and 1500 UTC, this results in the analysis of 9000 profiles of matched K_a- and W-band Doppler spectra.

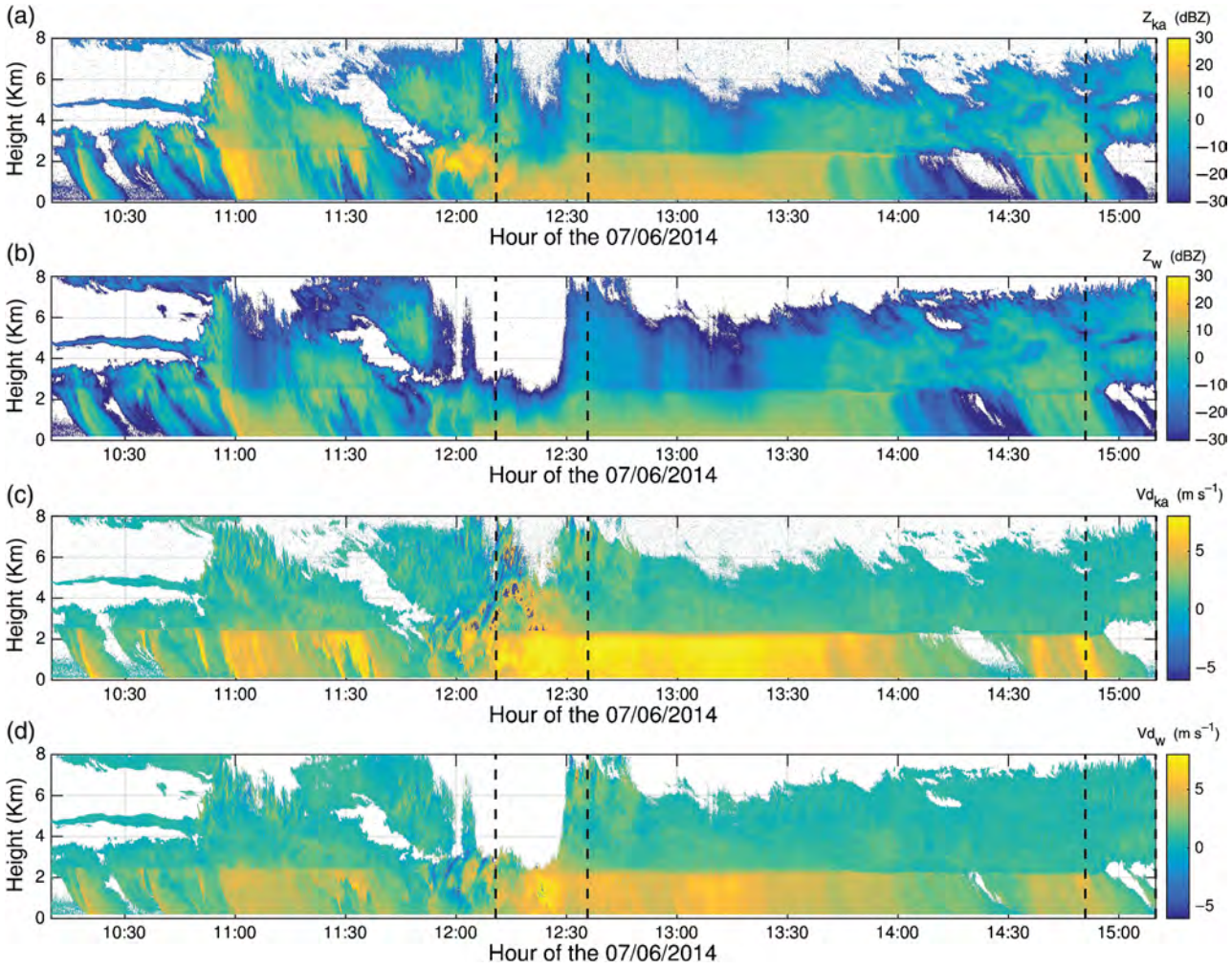

Figure 1. Time–height evolution of the (a, b) reflectivity and (c, d) mean Doppler velocity, for the (a, c) K_a-band and (b, d) W-band. Downward velocity is defined as positive and vertical lines indicate the periods when the X-SACR was operated in vertically pointing mode. [Colour figure can be viewed at wileyonlinelibrary.com].

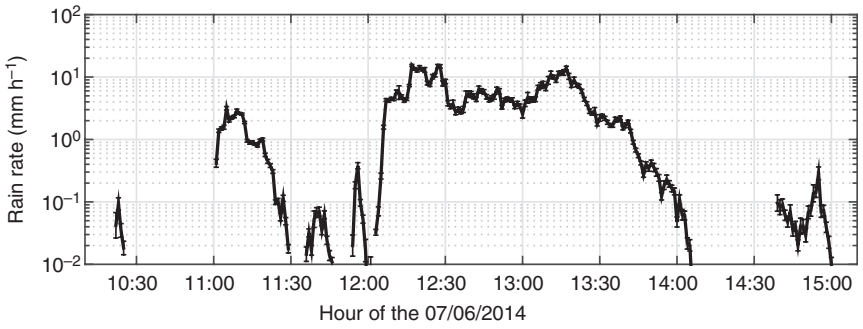

Figure 2. Evolution of the rain rate measured by the 2DVD. The errorbars correspond to the 1-sigma sampling statistical error computed according to (Testud *et al.*, 2001) .

3. Retrieval technique

DSD profiles are retrieved from multi-frequency Doppler spectra in a two-step approach, with two main outcomes in the first step (Tridon *et al.*, 2013a). Firstly, differences due to non-Rayleigh scattering observed in the measured Doppler spectra can be used to constrain the retrieval of the DSD shape, $N_{\text{shape}}(D)$. Secondly, by matching the Doppler spectra portion corresponding to Rayleigh scattering targets in the low velocity part of the spectrum, it is possible to estimate the K_a–W differential attenuation profile, $\Delta A(r)$, where r represents the range from the radars. The variable $N_{\text{shape}}(D)$ introduced here is a vector representing the relative concentration for each drop diameter D. No absolute concentration can be retrieved at this stage because the amount of rain and gas attenuation reducing the cloud radar reflectivity is not known. In the second step, the absolute DSDs are then retrieved by a combination of the two on a profile-to-profile basis. The rationale for the retrieval is illustrated in Figure 3 and is described in the next two sections.

3.1. *DSD shape*

The application of the optimal estimation scheme (Rodgers, 2000) to radar Doppler spectra analysis was originally proposed by Tridon and Battaglia (2015) and readers can refer to that article for full details. Here, the description is restricted to the essential parts with an illustration of its application for some observations of the case-study under consideration here, i.e. for two different heights of the profile measured at 1104 UTC (Figure 4).

At millimetre wavelength, scattering by rain drops depends on the frequency of the transmitted wave according to the Mie

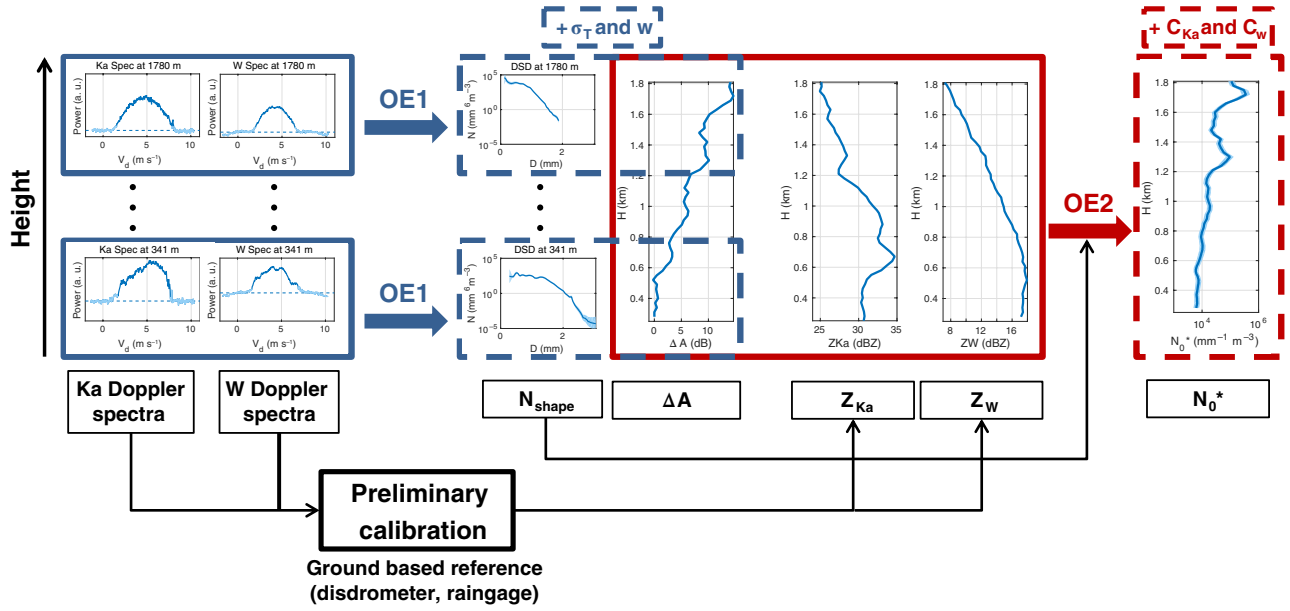

Figure 3. Schematic of the retrieval technique exemplified by a single observed profile. The retrieval consists of two optimal estimation steps, the first one applied at each range gate (framed by blue lines), and the second one applied on the whole profile (framed by red lines). For both steps, observations are framed by continuous line while retrieved quantities are framed by dashed lines. [Colour figure can be viewed at wileyonlinelibrary.com].

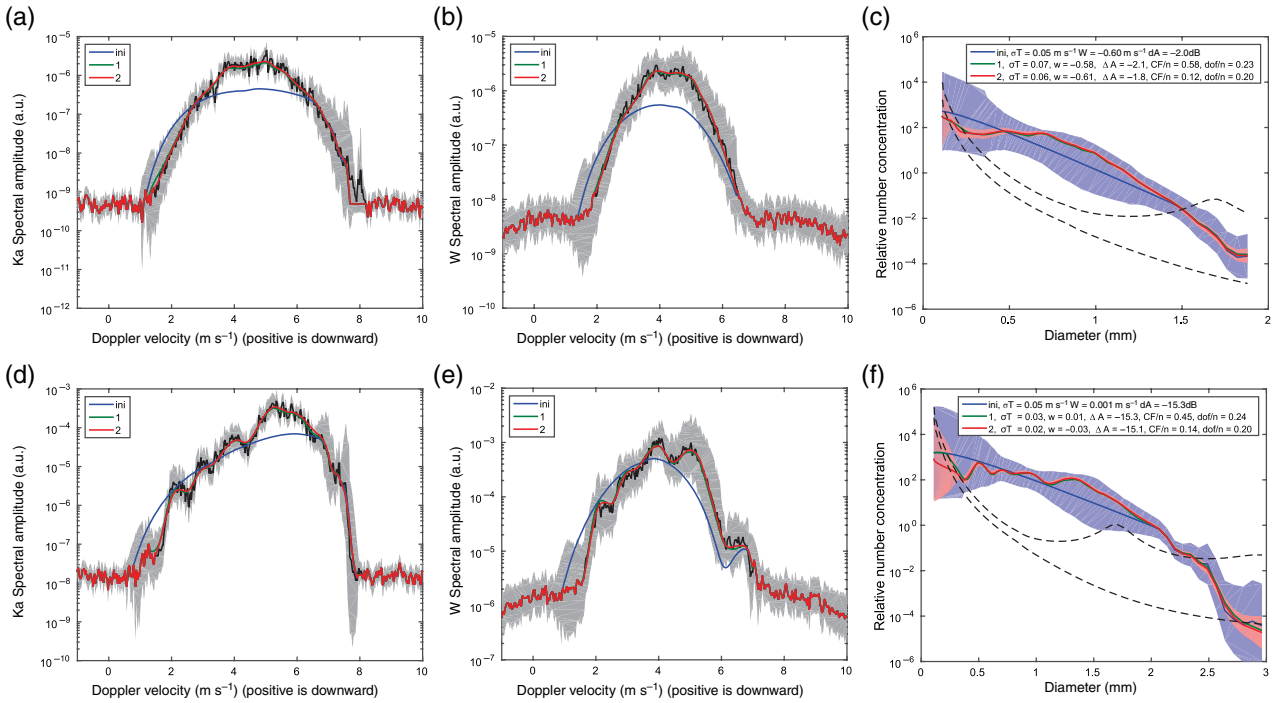

Figure 4. Illustration of the retrieval of the DSD shape at 1104 UTC for the lowest and highest heights: (a–c) 341 m and (d–f) 1780 m. The retrieval starts from the *a priori* (blue lines), tries to optimally match the observed K_a-band (black line in (a) and (d)) and W-band (black line in (b) and (e)) Doppler spectra, and converges after two iterations to the retrieved DSD shape (red line in (c) and (f)). Black shadings in (a, b, d, e) show the measurement errors while blue and red shadings in (c) and (f) show the error of the *a priori* and retrieved DSD, respectively. Thin dashed-black lines in (c) and (f) represent the DSD concentration corresponding to the Doppler spectra noise level, i.e. when the retrieved concentration falls below both lines, the measurements do not provide any information and the retrieval tends towards the *a priori* DSD. Miniatures of these panels are reproduced in Figure 3. [Colour figure can be viewed at wileyonlinelibrary.com].

theory (Lhermitte, 1990): the backscattering power oscillates with consecutive maxima and minima with increasing drop size and these oscillations modulate the Doppler spectrum with the possibility of producing multi-modal spectra at W-band. Figures 4(d) and (e) show a nice example of multi-modal spectra observed at K_a and W-band. While the modes observed by both radar (up to 5 m s^{-1}) are due to a multi-modal DSD, the last mode seen only by the W-band radar (above 6 m s^{-1}) can only be explained by the Mie oscillation of the backscattering cross-section. As such, Doppler spectra obtained from some of the largest drops can provide unique signatures of the drops sampled. For example, the position of the first minimum in the W-band backscattering cross-section corresponds to a raindrop terminal velocity of 5.9 m s^{-1} at sea level and its position in the observed Doppler spectra can be used to deduce the vertical air velocity (Kollias *et al.*, 2002; Giangrande *et al.*, 2010). However, the DSD shape cannot be uniquely deduced from a single Doppler spectrum because of spectral broadening caused by e.g. turbulence and vertical wind variability within the radar volume. The solution proposed by Tridon and Battaglia (2015) is to untangle the DSD shape from the broadening effect by combining the Doppler spectra observed at the two different radar frequencies. Best performances are obtained at low to moderate broadening when the Mie features are not smoothed out. In principle, once the vertical wind and turbulence have been estimated, the binned DSD shape can be retrieved from either of the two Doppler

spectra and the error is bin-independent and mainly driven by the random noise of the spectral reflectivity. In practice, the optimal estimation framework allows us to maximize the accuracy by retrieving all parameters simultaneously and matching both K_a- and W-band spectra at the same time.

When the drops are sufficiently small (diameter much smaller than the radar wavelength), the backscattering cross-section is the same at both frequencies and the Doppler spectra shape are similar at their small diameter end (e.g. Figures 4(a, b) and (d, e) up to $4\,m\,s^{-1}$). However, the absolute power measured for these range of diameters can stand apart because of a different calibration constant, a different radome attenuation, or a different attenuation caused by rain and gas present between the radars and the sampled volume. In general, the rain and gas attenuation increase with the radar frequency and the path-integrated differential attenuation therefore monotonically increases along the path.

The measurement vector is composed of each spectral reflectivity bins observed by the K_a- and W-band radars at the same position (e.g. Figures 4(a, b) and (d, e)). The DSD shape, $N_{shape}(D)$, is represented by n relative drop concentrations at n diameter bins D and does not assume any functional shape (e.g. Figures 4(c) and (f)). The state vector is composed of the n values of $N_{shape}(D)$, the mean clear air vertical velocity w ($m\,s^{-1}$), the air broadening spectral width σ_{air} ($m\,s^{-1}$) and the two-way path integrated differential attenuation ΔA (dB). Downward Doppler velocities are defined as positive in Figures 4(a), (b), (d) and (e), and in the remainder of the article.

From the state vector, it is straightforward to derive the measurement vector using the forward model described in Tridon and Battaglia (2015) which can produce Doppler spectra at any radar frequency, using a standard fall-velocity relation for drops (Atlas *et al.*, 1973), corrected for the change in air density with height. Using Gauss–Newton iterations, the objective is to find the state vector that minimizes a cost function between the measurement vector and the forward model in a least-squares sense. At each iteration, the cost function is linearized by computing the Jacobian matrix which contains the partial derivative of each observation with respect to each element of the state vector and is obtained via the perturbation method. Convergence is obtained after few iterations (two in Figure 4).

Since DSDs exhibit large spatial and temporal variability, a strong *a priori* constraint is necessary. A traditional DSD inversion technique provides a first guess with corresponding error which are both used as an *a priori* covariance matrix and as an initial condition of the iterative scheme (blue line and shading in Figures 4(c) and (f)). The covariance matrix of the measurements (black shading in Figures 4(a), (b), (d) and (e)) includes the forward model error which is mainly driven by the use of a fixed diameter–fall velocity relationship, and the random error of measured spectral reflectivity (which explains why Doppler spectra are noisy). In order to avoid reproducing the random measurement noise, a smoothness constraint is added to the retrieved drop concentration via a Twomey–Tikhonov regularization. The optimal choice of smoothness constant $\lambda = 10$ was found using the L-curve (not shown) technique (Pounder *et al.*, 2012).

One necessary condition for this retrieval is that sufficiently big drops are required to produce some detectable non-Rayleigh effect. However, observing a Mie notch in the W-band spectra is not absolutely necessary as Figures 4(a), (b), and (c) nicely illustrate. Indeed, on this example, significant differences between K_a and W-band spectra start at $4\,m\,s^{-1}$, which corresponds to raindrops of 0.8 mm, taking into account the vertical air motion retrieved for this case, and the air density reduction at this height. Generally, for rain rates as low as $0.1\,mm\,h^{-1}$, drops of 0.8 mm are always present in the DSD (e.g. compare Figures 2 and 10 for the rain event under study). Therefore, as will be shown later, the presence of detectable non-Rayleigh effects is not the main limitation for retrieving rain rates as low as $0.1\,mm\,h^{-1}$.

In summary, the profile of $N_{shape}(D)$ is retrieved by applying this optimal estimation technique (labelled as 'OE1' in Figure 3) to the K_a- and W-band Doppler spectra observed at each range gate taken independently (quantities framed in continuous blue lines). For clarity, the retrieved $N_{shape}(D)$ is shown for only two heights, but it is retrieved at any height with typical vertical resolution of 30 m. The full profile of retrieved ΔA (plotted inside the blue dashed box) shows a noisy behaviour since no vertical constrain has been imposed until now.

3.2. *Bulk rain properties*

A second step is necessary to retrieve the complete DSD. At each layer, the gas attenuation is computed using the model described in Rosenkranz (1998) and observations from the closest radiosounding, and is subtracted to the total differential attenuation, $\Delta A(r)$, thus providing the attenuation due to rain, $\Delta A_{rain}(r)$. Using the radiosoundings launched before (0522 UTC), during (1117 UTC) and after (1720 UTC) the rain event, the gas contribution of the cumulated differential attenuation within the rain layer differs by less than 0.1 dB (not shown). Therefore, the error due to the variation of the thermodynamic properties between each radiosounding can be considered negligible in comparison with the uncertainty on ΔA (about 0.5 dB).

In Tridon and Battaglia (2015), $\Delta A_{rain}(r)$ was directly used as a bulk constraint to compute the absolute concentration of the drops in $N_{shape}(D, r)$ using a scaling concentration factor $C_N(r)$. However, the retrieved rain attenuation can be very noisy, especially in the case of fine vertical resolutions and low rain rates.

In this work, a more generally applicable approach based on an additional optimal estimation step (labelled as 'OE2' in Figure 3 and illustrated in detail in Figure 5 for the full 1104 UTC profile) has been designed. It retrieves the absolute concentration of drops by matching the profiles of $\Delta A_{rain}(r)$ and of the observed radar reflectivity factors at the two frequencies, $Z_{K_a}(r)$ and $Z_W(r)$ (dB) (e.g. black lines in Figures 5(a) and (c), respectively). Compared to the previous methodology, the optimal estimation approach has the advantage of finding a more robust solution which best matches the whole $\Delta A_{rain}(r)$ profile. Similarly to the path-integrated attenuation technique used for satellite retrievals (e.g. Meneghini *et al.*, 2015), the knowledge of the attenuation produced by the whole rain layer provides a strong constraint and stabilizes the retrieval which is then less prone to retrieval errors. However, this new approach does require an absolute calibration of radar reflectivities, and therefore two additional unknowns, here referred to 'calibration adjustment' C_{K_a} and C_W (dB). They account for the possible absolute miscalibration of the radars, the radome attenuation and the attenuation from the radar to the first useful range bin (denoted later as r_{min}). The new retrieval framework has the advantage of optimally estimating the calibration adjustments in order to match both the attenuation profile and the measured reflectivity profiles.

As a result, the measurement vector for a single profile of m range gates is

$$y = \begin{pmatrix} Z_{K_a}(r_{min}) \\ \vdots \\ Z_{K_a}(r_m) \\ Z_W(r_{min}) \\ \vdots \\ Z_W(r_m) \\ \Delta A_{rain}(r_{min}) \\ \vdots \\ \Delta A_{rain}(r_m) \end{pmatrix} \quad (1)$$

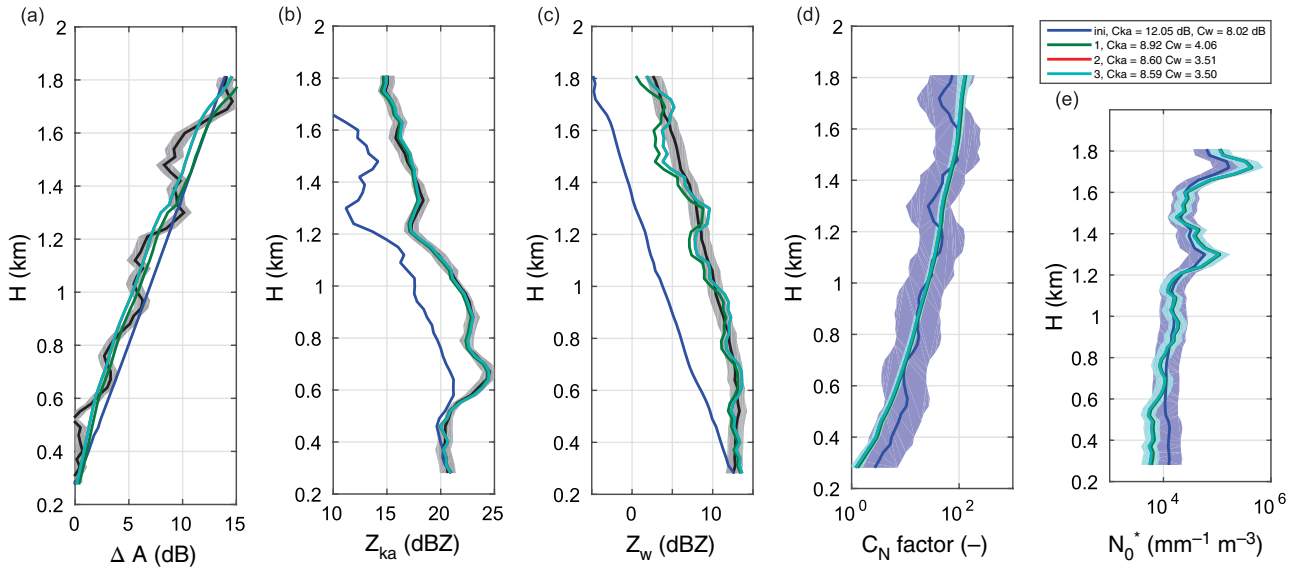

Figure 5. Illustration of the retrieval of the concentration parameter $C_N(r)$ at 1104 UTC for the full profile. The retrieval starts from the *a priori* (blue lines), tries to optimally match the diffential attenuation retrieved in OE1 (black line in (a)), and the K_a- and W-band reflectivity profiles (black line in (b) and (c)), and converges after three iterations to the retrieved $C_N(r)$ profile (cyan line in (d)). Black shadings in (a), (b) and (c) show the measurement errors while blue and cyan shadings in (d) and (e) show the error of the *a priori* and retrieved $C_N(r)$, respectively. The $N_0^*(r)$ profile corresponding to $C_N(r)$ at each iteration is shown in (e). Miniatures of these panels are reproduced in Figure 3. [Colour figure can be viewed at wileyonlinelibrary.com].

and the state vector is

$$x = \begin{pmatrix} \log C_N(r_{\min}) \\ \vdots \\ \log C_N(r_m) \\ C_{\mathrm{K_a}} \\ C_{\mathrm{W}} \end{pmatrix} \tag{2}$$

where $C_N(r_i)$ is a scaling concentration parameter which provides the full DSD $N(D, r_i)$ according to $N(D, r_i) = C_N(r_i) N_{\mathrm{shape}}(D, r_i)$; an example of a retrieved $C_N(r_i)$ profile is shown in Figure 5(d). The logarithm of $C_N(r_i)$ is used in order to avoid non-physical negative retrievals. As such, the forward model is straightforward: the reflectivity elements of the state vector are computed at each range gate r_i from the measurement vector according to Eq. (4), where $\Delta r = 30$ m is the vertical resolution of the observations, $|K_{\mathrm{W}}|^2 = 0.93$ is related to the complex refractive index of water at centimetre wavelengths, ν is the radar frequency and c is the speed of light. The backscattering and extinction cross-sections ($\sigma_{\mathrm{back},\nu}(D)$ and $\sigma_{\mathrm{ext},\nu}(D)$, respectively) are computed by the T-matrix method assuming an axial ratio-diameter relationship (Beard and Chuang, 1987). Equation (5) is used to compute the differential attenuation elements using

$$\Delta A_{\mathrm{rain}}(r_i) = A_{\mathrm{rain,W}}(r_i) - A_{\mathrm{rain,Ka}}(r_i). \tag{3}$$

From these equations, the Jacobian matrix can be computed analytically. Therefore, the covariance matrix of the measurements does not include any model error: $\Delta A_{\mathrm{rain}}(r)$ error is derived from the $\Delta A(r)$ error retrieved during the first step, and the random error of reflectivity measurements is estimated using the corresponding signal-to-noise ratio and spectrum width following Hogan *et al.* (2005) (black shadings in Figures 5(a)–(c)). As in the first step, a Twomey–Tikhonov regularization smoothes out the random noise of the measured reflectivity and differential attenuation profiles.

The *a priori* covariance matrix and the initial condition of the iterative scheme are provided by a first guess coming from a simplified retrieval (blue shading in Figure 5(d)). Here, a choice is made between two schemes according to the total differential attenuation of the profile:

- If $\Delta A_{\mathrm{rain}}(r_m) > 4$ dB (i.e. medium/high rain rate), the differential attenuation contains enough information to constrain the retrieval of the absolute concentration of drops and of the calibration adjustment as well. Then, $C_N(r_i)$ first guess and its covariance are computed at each level by inverting the derivative of Eq. (3) at level r_i, while the calibration constants are deduced from Eq. (4) at the level $r_{\min}$. Since this procedure is not very accurate, the errors on the calibration constants *a priori* are fixed to large values of 5 dB. These conditions represent the optimal range for the applicability of the retrieval and corresponds to those illustrated in Figure 5.
- Otherwise (i.e. light rain), ground-based instruments like rain gauges or disdrometers – instruments routinely operated at ARM sites – are necessary to provide a first-guess absolute reflectivity calibration. This is a challenging task during rain due to antenna or radome wetness (Hogan *et al.*, 2003). Then, $C_N(r)$ first guess and its covariance are deduced from calibrated $Z_{\mathrm{K_a}}(r)$ using Eq. (4) in an iterative procedure from the lowest to the highest measurements similarly to what is done in Peters *et al.* (2005, 2010). Such schemes are more suited to low rain rates where attenuation is weak because errors can quickly amplify with range. For this reason, the K_a-band reflectivity profiles are used rather than the W-band reflectivity profiles, and including $\Delta A_{\mathrm{rain}}(r)$ profile in the optimal estimation measurements vector binds the attenuation to realistic values. However, convergence still relies on a well-constrained calibration constant *a priori*, the error of which is set to 0.1 dB.

$$Z_\nu(r_i) = 10 \log \left(C_\nu \frac{(c/\nu)^4}{\pi^5 |K_{\mathrm{W}}|} C_N(r_i) \int_0^{D_{\max}} N_{\mathrm{shape}}(D, r_i)\, \sigma_{\mathrm{back},\nu}(D)\, \mathrm{d}D \right) - A_{\mathrm{rain},\nu}(r_i), \tag{4}$$

with

$$A_{\mathrm{rain},\nu}(r_i) = \frac{20}{\ln 10} \left(\int_{r_0}^{r_{i-1}} \int_0^{D_{\max}} C_N(r) N_{\mathrm{shape}}(D, r) \sigma_{\mathrm{ext},\nu}(D)\, \mathrm{d}D\mathrm{d}r + \frac{\Delta r}{2} \int_0^{D_{\max}} C_N(r_i) N_{\mathrm{shape}}(D, r_i) \sigma_{\mathrm{ext},\nu}(D)\, \mathrm{d}D \right). \tag{5}$$

The use of the Twomey–Tikhonov regularization guarantees smooth retrievals in the vertical, with the optimal smoothness constant $\lambda = 10^4$ found using the L-curve technique like in the first step of the retrieval. However, at the very last stage of the retrieval, $N_0^*(r)$ is deduced from $C_N(r)$ and $N_{\text{shape}}(D,r)$ according to Testud *et al.* (2001):

$$N_0^*(r) = C_N(r)\frac{4^4}{\Gamma(4)}\frac{\left[\int_0^{D_{\max}} D^3 N_{\text{shape}}(D,r)\mathrm{d}D\right]^5}{\left[\int_0^{D_{\max}} D^4 N_{\text{shape}}(D,r)\mathrm{d}D\right]^4}, \qquad (6)$$

which may lead to slightly noisy $N_0^*(r)$ profiles since $N_{\text{shape}}(D,r)$ is retrieved at each range gate independently. In order to minimize this effect, the rare outliers in $N_{\text{shape}}(D,r)$ profiles are carefully filtered before applying OE2 by looking at continuity in the w, σ_{air}, ΔA and D_m profiles. Despite this, and the fact that OE2 is applied to each profile independently, the retrievals show a very good consistency from gate to gate and from profile to profile (Figure 7).

These results can be further improved by combining the two steps of this retrieval in a single huge OE scheme applied to a whole profile, once the correlation distances of the different parameters involved will be better known. However, this is kept for future work since in its current state the retrieval is already computationally demanding. For example, the retrieval of a single profile of DSDs takes an average 50 min of CPU time and therefore, the 9000 profiles of this case-study could only be reasonably processed by using a high number of parallel computations on a supercomputer.

4. Results

The rain retrieval described in section 3 has been applied to the whole 7 June 2014 event, stopping at a height of 1.8 km above ground level (agl), in order to avoid possible contamination by melting hydrometeors (Figure 1). The first step, applied to each grid point independently, retrieves w, σ_{air} and ΔA (Figures 6(a)–(c)) as well as the DSD shape, $N_{\text{shape}}(D)$. For the sake of clarity, only the mean volume diameter D_m is shown in Figure 6(d) with

$$D_m(r) = \frac{\int_0^{D_{\max}} D^4 N_{\text{shape}}(D,r)\,\mathrm{d}D}{\int_0^{D_{\max}} D^3 N_{\text{shape}}(D,r)\,\mathrm{d}D}. \qquad (7)$$

Note that the expression of D_m is independent of $C_N(r)$. Then, the second step combines each retrieved ΔA and $N_{\text{shape}}(D,r)$ profiles in order to retrieve the full DSD $N(D,r)$ from which the concentration parameter $N_0^*(r)$ (Figure 6(e)) is deduced using Eq. (6). From the full DSD, any moment such as rain rate (Figure 6(f)) can be computed.

All the retrieved fields in Figure 6 present realistic and coherent structures. The first step of the retrieval converges practically everywhere, provided that the signal of both radars is significantly above noise. For narrow DSDs and highly variable rainfall, the possible volume mismatch between the two radars can seriously degrade the retrieval. During the BAECC campaign, even though great care was taken to align the radars to the zenith direction during their installation, a small 1° mispointing of the MWACR was discovered in a previous multi-frequency Doppler spectra study (Kneifel *et al.*, 2016). All these reasons possibly explain why the retrieved parameters become noisy before 1100, between 1120 and 1200, and after 1400 UTC. σ_{air} is particularly challenging to retrieve and appears very noisy. This is not surprising since its signature in dual-frequency Doppler spectra is weak and can be strongly affected by the volume mismatch of the two radars.

Several interesting features are retrieved in this rain event.

- In Figure 6(a), showers and light rain (e.g. before 1100 and after 1400 UTC) are embedded in some slightly positive vertical wind; while moderate updraughts (downdraughts) up to $4\,\mathrm{m\,s^{-1}}$ around 1200 UTC ($-2\,\mathrm{m\,s^{-1}}$ around 1230 UTC) are observed in the convective part, only weak vertical winds (between -0.5 and $1\,\mathrm{m\,s^{-1}}$) are observed in the stratiform part between 1230 and 1400 UTC.
- In Figure 6(b), the patches of high σ_{air} between 1200 and 1230 UTC are probably due to some strong local turbulence. However, σ_{air} values are always smaller than $0.5\,\mathrm{m\,s^{-1}}$. Larger σ_{air} identified as problematic in Tridon and Battaglia (2015) seem to be very rarely reached. The retrieved σ_{air} suggests that the retrieval of this parameter becomes increasingly troublesome at small D_m. Indeed, if the differences between K_a- and W-band Doppler spectra are too weak (i.e. the Mie effects are not detectable), the retrieval technique cannot disentangle the σ_{air} effect from $N_{\text{shape}}(D)$. For such periods, other retrieved parameters, such as D_m, must be interpreted cautiously, but are probably still sensible. Indeed, σ_{air} is generally very small compared to the spectrum width of the DSD, σ_{DSD} (Borque *et al.*, 2016).
- In Figure 6(c), D_m reaches fairly large values of up to 2.5 mm in both the stratiform and convective parts. In the convective part these large D_m are likely the consequence of some drop sorting due to the successive updraughts and downdraughts. The evolution of the DSD at 1000 m between 1223 and 1229 UTC (Figure 7(a)) corroborate this assumption with larger drops seen first. In the stratiform part, such large D_m which are already present close to the melting level are the signature of aggregation processes of ice particles occurring above or within the melting layer. A recently proposed technique (Matrosov, 2017) retrieves D_m directly from the Doppler velocity difference between K_a- and W-band, therefore neglecting the effect of turbulence broadening and the DSD shape variability. Because of the assumptions used in this procedure, the retrieval of D_m is limited to values between 0.5 and 1.8 mm. This is clearly a limiting factor for the rain event under study, with important portions where no retrieval is available in both stratiform and convective parts. Future work will aim at comparing the performances of these two techniques on an extended dataset.
- The retrieved ΔA reaches fairly high values of up to 20 dB during the heaviest rain (Figure 6(d)). For reference, the component due to gas is only about 1.4 dB at 3 km. Liquid clouds can also produce significant one-way attenuation of $5\,\mathrm{dB\,km^{-1}(g\,m^{-3})^{-1}}$ (Battaglia *et al.*, 2014). A collocated ceilometer detects the presence of some intermittent clouds at varying heights (black dots). Their base is used to flag the situations where caution must be taken in the interpretation of the retrieval of R and N_0^*. However, no obvious step in ΔA is observed corresponding to cloud base changes, suggesting that these cloud layers should not have a considerable liquid water content. This is somehow generally expected since cloud layers in rain can be rapidly depleted through droplet collection.
- High-resolution (every 2 s) N_0^* profiles like in Figure 6(e) are a first in rain remote-sensing studies. This event presents a variety of N_0^* values in good agreement with the range observed by Testud *et al.* (2001). Accordingly, larger values are retrieved during the convective shower between 1100 and 1130 UTC than in the stratiform rain. In general, N_0^* is constant with height but it can also be decreasing towards the ground (e.g. between 1100 and 1130 and around 1315 UTC). In combination with a decrease in rainfall rate (Figure 6(f)), this is believed to be a signature of evaporation that causes small drops to evaporate at a faster rate, leading to an increase of D_m (Kumjian *et al.*, 2010). In stratiform rain, this signal is rather weak because the loss of small drops can be partially compensated by an efficient break-up process. On the other hand, the loss

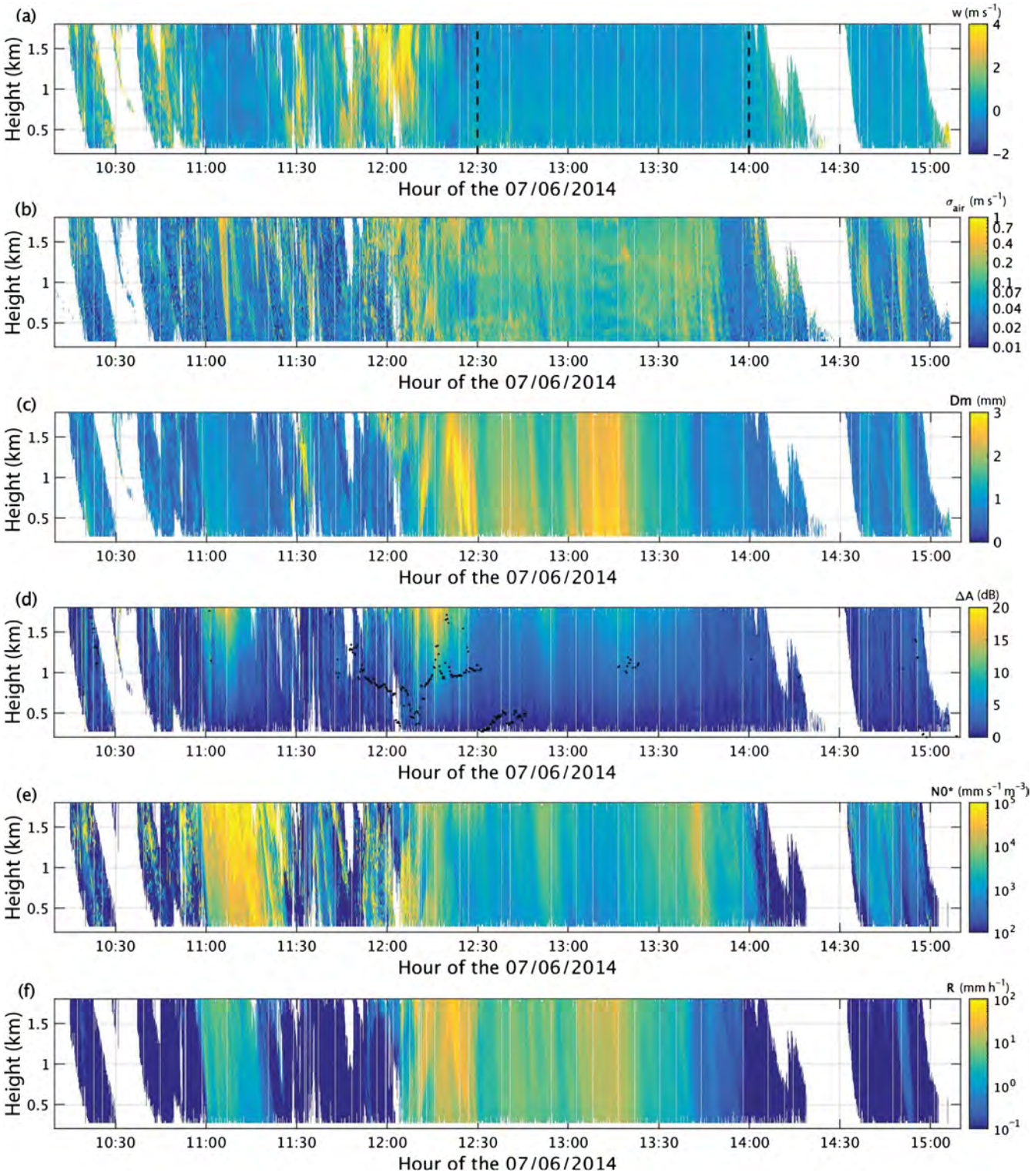

Figure 6. Time–height evolution of some of the retrieved parameters: (a) vertical wind w (positive is upward), (b) air broadening spectral width σ_{air}, (c) mean volume diameter D_m, (d) two-way path integrated differential attenuation ΔA, (e) concentration parameter N_0^* and (f) rain rate R. The vertical lines in (a) indicate the period used for comparison in section 5.1. The black dots in (c) show the retrieved positions of clouds layers detected from observations of a collocated lidar. [Colour figure can be viewed at wileyonlinelibrary.com].

of small drops is clearly visible at 1109 UTC (Figure 7(b)) where, the rain rate is low (3 mm h^{-1}), there are no drops larger than around 2 mm, and therefore break-up should remain scant (McFarquhar, 2004). However, in this type of rain, drop sorting could also play a non-negligible role. Future work will aim at getting a better insight into these different microphysical processes. For this, the rain volume can be decomposed into a drop number concentration and a corresponding DSD mean size and breadth (Williams, 2016).

5. Validation

The accuracy of the retrieved parameters can be evaluated thanks to the comparison with other retrievals or additional instruments. Firstly, the retrieval of vertical air motion is validated (section 5.1) thanks to comparison with the results of another technique using the W-band radar only. Secondly, the retrieved DSDs at the ground (section 5.2) and their corresponding moments (section 5.3) are validated against observations from the 2DVD. Finally, vertical profiles can be validated via intercomparisons

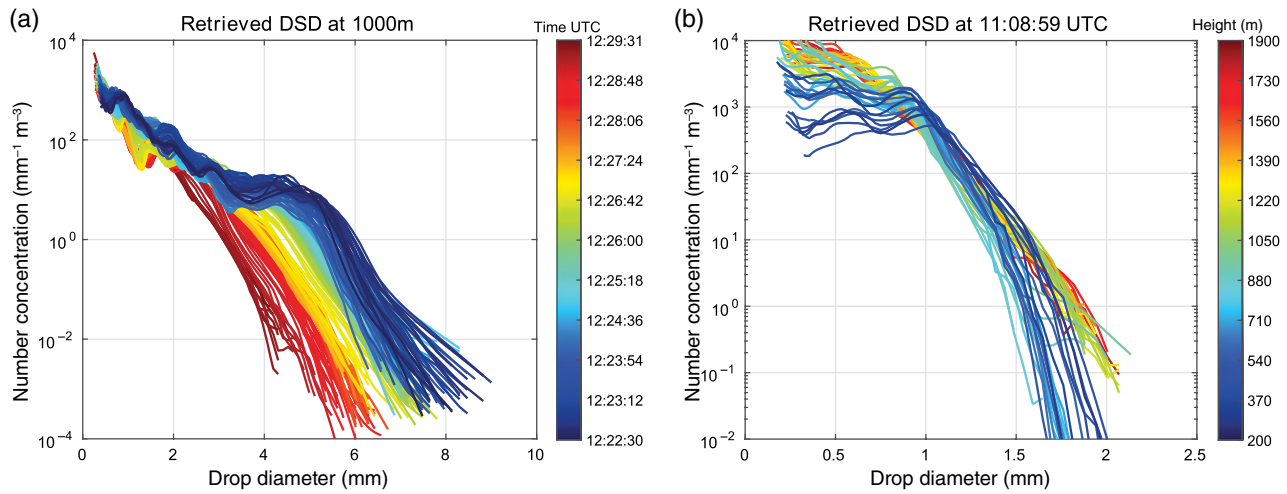

Figure 7. Examples of retrieved DSDs showing the temporal and vertical consistency of the retrieval at its full resolution: (a) evolution of DSDs retrieved every 2 s at 1000 m between 1222:30 and 1229:31 UTC, and (b) profile of DSDs retrieved every 30 m at 1108:59 UTC. [Colour figure can be viewed at wileyonlinelibrary.com].

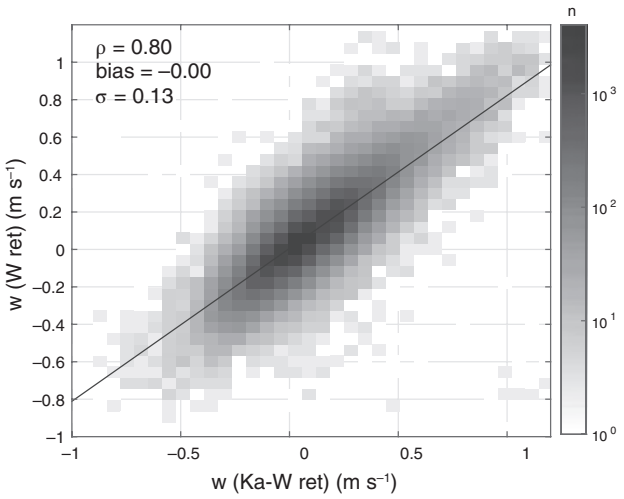

Figure 8. Scatterplots of vertical air motion retrieved using the K_a–W band combination versus the W-band only technique.

with the collocated X-SACR whose observations can be forward modelled from the microphysics profiles (section 5.4).

5.1. *Vertical air motion*

As mentioned in section 3, Kollias *et al.* (2002) and Giangrande *et al.* (2012) demonstrated that Mie backscattering oscillations are observed in the Doppler spectra of vertically pointing W-band radars in rain. They used the location of the first notch in the Doppler spectra as an anchor point to retrieve the vertical air motion with an accuracy of about 10 cm s^{-1}. This single-frequency technique has been applied to the stratiform period of the present case between 1230 and 1400 UTC as indicated by the vertical dashed lines in Figure 6(a) and its results are compared with the dual-frequency retrieval in the scatterplot of Figure 8. The agreement is good, with a negligible bias and a standard deviation of 13 cm s^{-1}, confirming the accuracy of roughly 10 cm s^{-1} for both techniques. Such results are not surprising since both techniques make use of the specific non-Rayleigh features observed in the W-band Doppler spectra. However, the single-frequency technique has the great advantage of being unaffected by any cross-instrument volume mismatch while the dual-frequency technique has the advantage of being potentially applicable to any DSD.

Outside the 1230–1400 period, the single-frequency technique reaches its limit of applicability since the first minimum in the W-band Doppler spectra is not clearly identifiable either because large enough drops are not present in the sampling volume, or because of the multimodality of the DSD. For example, for the W-band spectrum observed at 1205 at 1.6 km (orange curve in Figure 9(a)), the single-frequency technique is confronted with the ambiguity of the deep valley located near 2 m s^{-1} and what could appear to be a poorly defined non-Rayleigh notch at 4 m s^{-1} (highlighted by the black circle). Since no Mie oscillations are expected at K_a-band, the K_a-band spectrum (blue curve in Figure 9(a)) indicates that the corresponding DSD is multimodal, with minima caused by a lack of drops at their corresponding diameters, probably because of a drop-sorting effect induced by the strong dynamics present at this time. The corresponding K_a- over W-band Doppler spectra ratio (DSR; Figure 9(b)) introduced by Tridon *et al.* (2013a) agrees clearly with the ratio of the backscattering cross-section predicted by Mie theory (thick red dashed line). The DSR peak position is unambiguously identified and therefore the air motion can be retrieved by the dual-frequency technique with the same accuracy, even in case of very pronounced multimodal DSDs; the retrieved DSD for these spectra is shown in Figure 9(c). With an accuracy of the order of 10 cm s^{-1}, such vertical wind estimates are good enough to allow the retrieval of drop concentration with reasonable errors (Atlas *et al.*, 1973).

5.2. *Full DSD*

The 2DVD samples each individual drop passing through its 0.1 m^2 measuring area and provides the concentration of drops per 0.2 mm diameter bin every minutes (Kruger and Krajewski, 2002). In order to remove suspicious measurements (due to splashing, multiple drops in a sample, insects, etc.), observed drops are filtered according to the Atlas *et al.* (1973) fall velocity–diameter relationship. Figure 10(a) shows the evolution of the DSD at the ground as measured by the 2DVD. The DSD is highly variable in time and the concentration of drops decreases quickly with size. Because of the small sample volume of the instrument, few drops are sampled during the 1 min integration time, in particular for large diameters, which explains the noisiness of this part of the DSD.

For a meaningful comparison, the retrieved DSDs at the lowest range gate are averaged over 1 min to match the temporal resolution of the 2DVD (Figure 10(b)). Since the lowest available radar gates are at r_{min} = 280 m agl, the time required by the drops to reach the ground can produce a non-negligible temporal shift between retrievals and observations, in particular for light rain. The correction of this temporal shift for each individual diameter is a challenging task and can worsen the results. A simple and robust solution is to apply a time correction to each DSD as a whole, assuming a fall velocity

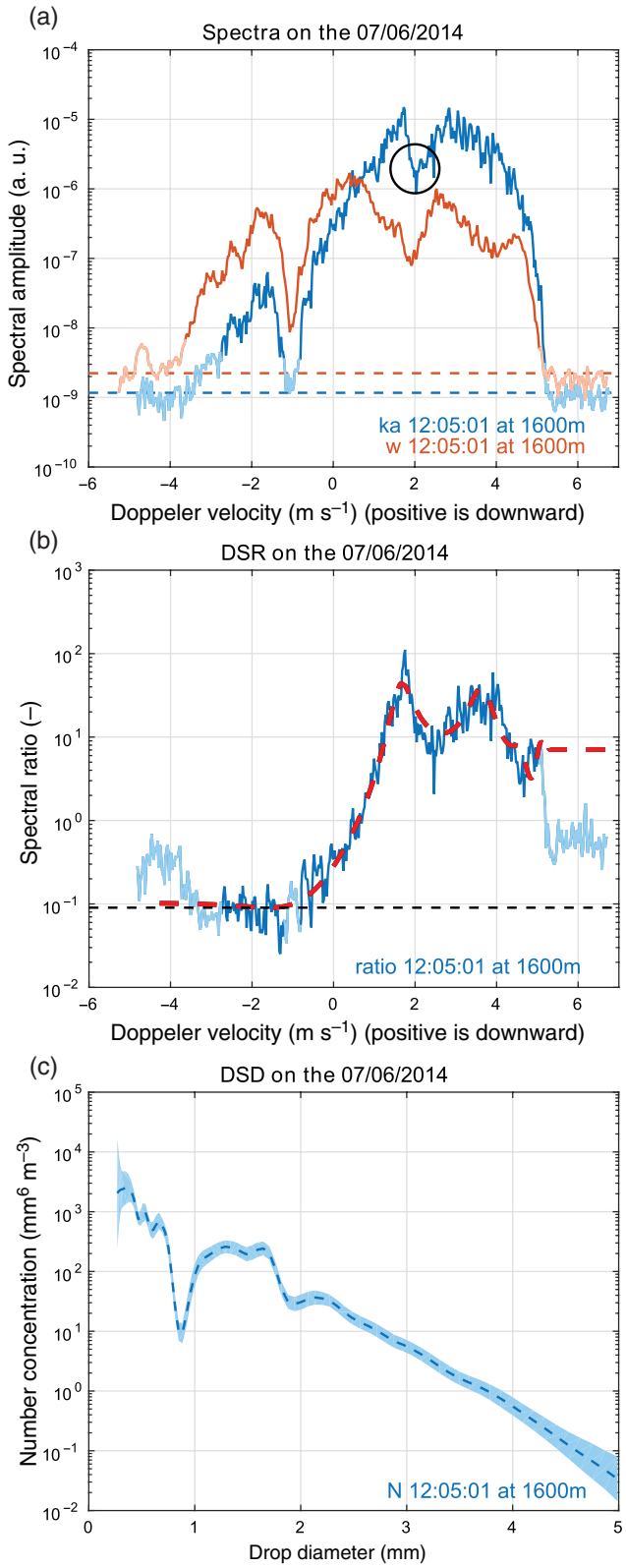

Figure 9. (a) Doppler spectra observed by K_a- and W-band on 7 June 2014, (b) corresponding Doppler Spectra Ratio (DSR; the ratio of the K_a- over the W-band Doppler spectra) and (c) retrieved drop size distribution (DSD) at 1205 UTC and 1.6 km. In (a) and (b), the lighter parts of the lines highlight the weak fractions of the signal which are not further used in the retrieval. [Colour figure can be viewed at wileyonlinelibrary.com].

corresponding to its mean volume diameter D_m according to $T_{\text{shift}} = r_{\min}/\{V(D_m) - w(r_{\min})\}$ where $w(r_{\min})$ is the retrieved vertical wind at the lowest range gate. This imperfect correction is not ideal for the smallest drops since they can have much longer time shifts, but will provide best results for diameters close to D_m, and DSD moments dominated by these range of diameters like D_m, R and N_0*. In case of very light rain and/or updraughts, the time shift can be long or negative and is therefore restricted to values between 0 and 10 min (only 20 occurrences outside this range in about 7000 DSDs).

Overall, the agreement between the observed and retrieved DSD is excellent (compare Figures 10(a) and (b)). The most remarkable differences are at large diameters where the retrieved DSDs are much smoother. These differences translate into the median volume diameter D_0 (thick black lines) reaching a maximum of 2.25 and 2.5 mm for the observed and retrieved DSDs, respectively. Two possible reasons can explain these discrepancies:

(i) the scarcity of these large drops is real and the smooth behaviour of the retrieved DSD is due to a 1 mm correlation length between drop concentration imposed in the optimal estimation, or

(ii) the drop number concentration at these diameters is too small to provide a reliable number concentration in the small sampling volume of the 2DVD.

Future work on a larger dataset will aim at more deeply understanding these discrepancies.

In Figure 11, DSDs at 1117, 1219 and 1306 UTC exemplify the performance of the retrieval. The uncertainty of both DSD estimates are represented as black errorbars for the 2DVD (computed according to Testud *et al.*, 2001) and as blue/grey shading for the optimal estimation. Given the considerable volume mismatch between the observed and the retrieved DSD, the agreement is remarkable. In particular, Figures 11(b) and (c) highlight the capability of the Doppler spectra technique to retrieve multimodal and more realistic DSDs at large raindrop diameters, respectively.

During the initial shower between 1100 and 1130 UTC, there is a remarkable agreement between the retrieval and 2DVD observations for drops larger than 0.7 mm (Figures 10 and 7(a)). Interestingly, a very high concentration of very small drops ($D \approx 0.25$ mm), in line with observations of Testud *et al.* (2001) for such diameters, is retrieved but not seen by the 2DVD. It is well known that the sensitivity of disdrometers is limited for small drops (Tokay *et al.*, 2013). Looking at Figure 10, the decrease of concentration for drops smaller than 0.5 mm recorded by the 2DVD is questionable. A possible explanation is the very small terminal velocity of these drops, which makes their signal challenging to interpret because the shadow they produce on the two 2DVD cameras cannot be easily matched (Thurai *et al.*, 2014). On the other hand, the presence of large drops seems to be correlated with high concentration of small drops in 2DVD observations (e.g. at 1225 and 1315) but not in the retrieval which suggests a possible artifact in the 2DVD observations. This highlights another domain where the retrieval seems to outperform the 2DVD capabilities.

More observations for other cases and locations are required in order to confirm these results and to conclude for which specific range the retrieval provides the best results. On the other hand, the observed discrepancies with the 2DVD are scarce, affect only the small-drop end of the spectrum and have a small effect on the high moments of the DSD (namely D_m, N_0* and R) which are of interest for the rain observation community. Therefore, this single case highlights the general good agreement between the retrieval and disdrometer observations. However note that accurate estimates of the concentration of drops (zeroth moment of the DSD) is fairly difficult to obtain from any observations, while it is generally required in rain parametrizations.

5.3. *DSD moments*

Figures 12 and 13 show the temporal evolution and the scatterplots of the observed and retrieved DSD moments D_m, N_0^* and R, respectively. The agreement for D_m is particularly good (Figure 12(a)) knowing that its retrieval is fully independent of the 2DVD observations. Indeed, D_m can be determined from

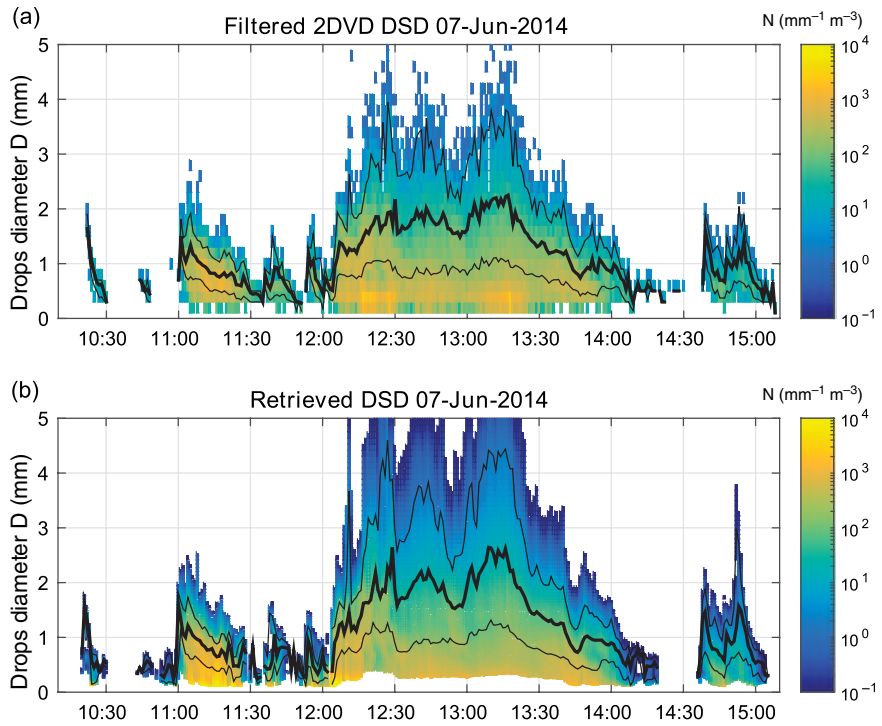

Figure 10. Evolution of the DSDs observed on 7 June 2014 (a) by the disdrometer at the ground and (b) retrieved at 300 m agl. The black lines are the diameters corresponding to the 10th, 50th and 90th percentiles of the total rain volume. [Colour figure can be viewed at wileyonlinelibrary.com].

Eq. (7) directly after the first step of the retrieval, which performs well even for light rain. Similarly to D_0, the discrepancies observed for large D_m are likely due to the sampling limitations of the 2DVD. The corresponding correlation, bias and standard deviation (Figure 13(a)) are very good with values of 0.96, 0.02 and 0.19 mm, respectively. These metrics are similar to those of the retrieval based on wind profiler data on a long-lasting stratiform rain event (Williams, 2016).

The N_0^* calculation (Eq. (6)) requires the retrieval of the complete DSD and is therefore done in the second step of the retrieval. As described in section 3.2, this retrieval is applicable to two regimes with different levels of accuracies. For high rain rates, the differential attenuation between K_a- and W-band radars provides a very good signal (absence of grey shading in Figure 12(b) corresponding to cumulative K_a−W differential attenuation values larger than 4 dB). Otherwise, the retrieval relies on a prior calibration adjustment using the disdrometer, which is known to be uncertain in particular for very light rain. Overall, a reasonably good agreement is found for the whole event (Figure 12(b)). Since N_0^* can vary over several orders of magnitudes, statistics are built considering observed and retrieved N_0^* (mm^{-1} m^{-3}) in decibels (dBN). However, this gives a lot of weight to the small N_0^* corresponding to very light rain. Therefore, the scatterplot of Figure 13(b) shows N_0^* values associated with rain rates larger than 0.01 mm h^{-1} only, giving correlation, bias and standard deviation of 0.94, −0.93 and 2.11 dBN, respectively. Note that the excluded values have a very small contribution to rain rate and total accumulation and would have produced marginal errors on N_0^* if considered in linear units.

Finally, in terms of rain rate, the retrieval shows a fairly good agreement over the full range of values from 0.1 to 16 mm h^{-1} (Figure 12(c)). Similarly to N_0^*, the retrieval of R in the grey shading periods requires a calibration adjustment with a disdrometer. However, these correspond to very low rain rates (mainly $R < 1$ mm h^{-1}). Overall, the corresponding correlation, bias and standard deviation are very good with values of 0.97, 0.04 and 0.93 mm h^{-1}, respectively (Figure 13(c)).

Another innovative technique exploiting cloud radar for the retrieval of rain rate (Chandra *et al.*, 2015) has been applied to this event. It makes use of the close relation between rain rate and attenuation at K_a band (Matrosov, 2005). Its main advantage is that it is based on the observations of a single radar and is therefore unaffected by any cross-instrument volume mismatch. However, for low attenuation (i.e. low rain rate), it relies on a reflectivity–rain rate relation and is therefore affected by radome attenuation as well. For a fair comparison, it was applied to the K_a band reflectivity after the calibration adjustment with the disdrometer. This K_a-band-only retrieval provides good results (correlation, bias and standard deviation of 0.78, 0.01 and 2.47 mm h^{-1}, respectively, Figure 13(c)) but is outperformed by the dual-frequency retrieval. As predicted by Tridon *et al.* (2013b), the main limitation of the single-frequency technique is the assumption that vertical changes in microphysical properties are weak within 500 m thick layers. As proposed by Chandra *et al.* (2015), this issue can be mitigated by averaging radar observations over 1 min, but this seems insufficient for the current case-study. Indeed, in the case of high horizontal wind or wind shear, fallstreaks of precipitation can be significantly tilted (Figure 1) and present highly variable microphysical properties in the vertical for periods longer than 1 min (visible in Figures 6(d)–(f) during the showers before and after the main rain event).

5.4. *X-band comparison*

Following Tridon and Battaglia (2015), once the DSD, the vertical wind and the air broadening are known, the radar Doppler spectra can be forward modelled at any frequency, using the corresponding scattering and extinction cross sections and assuming a similar radar beam width. From the obtained Doppler spectra profiles, the profiles of reflectivity, Doppler velocity and spectral width can be computed. In Figure 14, such profiles simulated at X-band are compared with X-SACR observations. A remaining unknown is the radome attenuation suffered by the X-SACR. Therefore, similarly to K_a and W-band radars, a calibration adjustment was determined from 2DVD observations in order to correct X-SACR reflectivity profiles. Because of the height difference between the first radar gate and the 2DVD, this process is uncertain, and can alter the evaluation of the retrieval performance, in particular for non-steady rain.

The X-SACR was operated in vertically pointing mode during two distinct periods (highlighted by the vertical dashed lines in Figure 1): during heavy convective rain between 1210 and

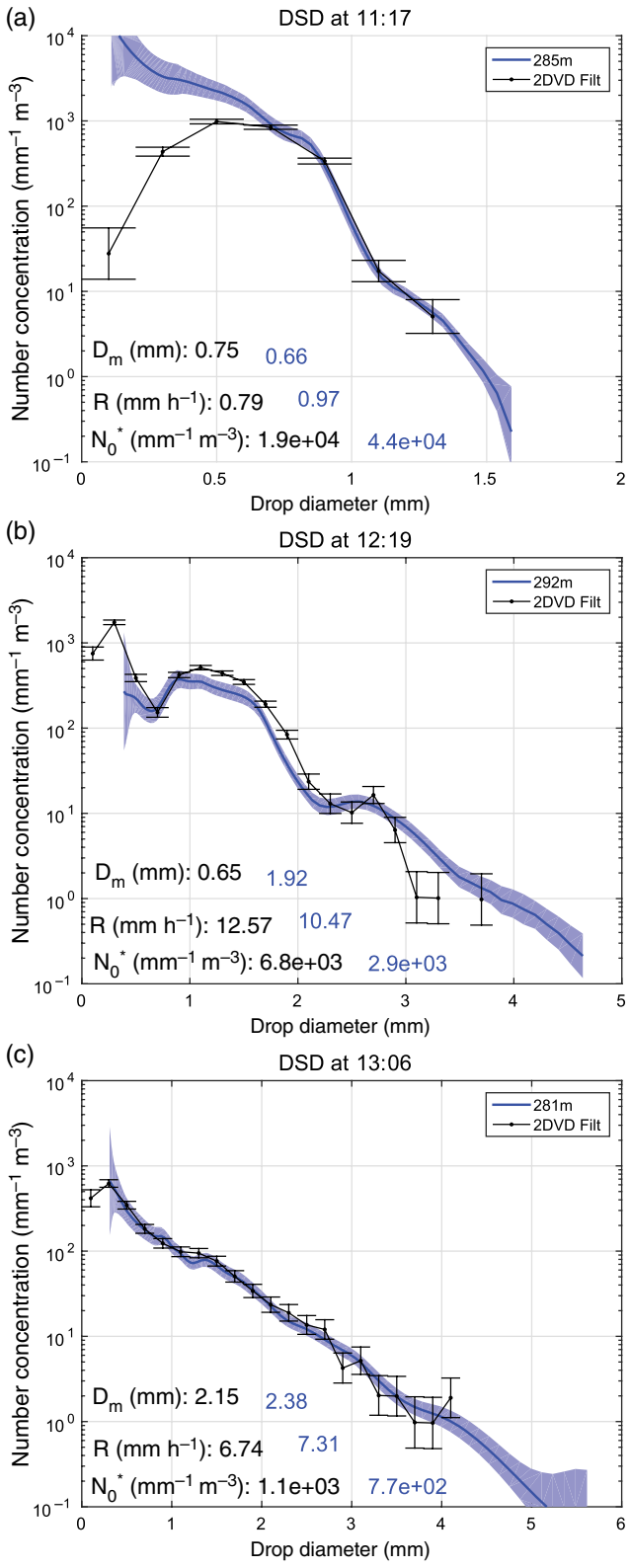

Figure 11. Comparison of the DSD retrieved (blue/grey line and shading) and the DSD observed by the 2DVD (black errorbars) at (a) 1117, (b) 1219 and (c) 1306 UTC. [Colour figure can be viewed at wileyonlinelibrary.com].

1235 UTC, and during decaying light stratiform rain after 1450 UTC. The reflectivity corresponding to these two periods splits into two different clusters below and above 30 dBZ in Figure 14(a). The more significant scatter at large reflectivities is probably due to the high variability of convective rain combined with the much larger beamwidth of the X-SACR (1.2°). For the low reflectivity cluster (light stratiform rain), the scatter is much smaller but a bias is visible, in particular between 10 and 25 dBZ. Such a bias can easily be explained by the particularly challenging calibration adjustment: in such decaying light rainfall, the weak Doppler velocity (lower than 4 m s^{-1} for K_a-band; Figure 1) implies a significant time to fall from the radar gate to the ground, during which rainfall can be seriously affected by evaporation. Since the retrieval relies on the preliminary calibration adjustment for this kind of rainfall (differential attenuation is practically negligible), this calibration can be uncertain for any of the three radars and is probably the cause of this bias. Nevertheless, the overall agreement between simulated and observed X-band reflectivity is very good with correlation, bias and standard deviation of 0.99, 0.85 and 2.37 dB, respectively.

The comparison between simulated and observed X-band Doppler velocity (Figure 14(b)) provides fairly good results (correlation, bias and standard deviation of 0.97, 0.11 and 0.5 m s^{-1}, respectively) and no bias is visible over the whole range of Doppler velocities. Since by definition, the mean Doppler velocity is independent of any miscalibration issue, the absence of bias is expected and suggests the good performance of the retrieval of vertical wind and $N_{\text{shape}}(D)$. Furthermore, this confirms that the bias observed in the reflectivity scatterplot is mainly due to miscalibration. Similarly, the larger scatter at large Doppler velocities can be explained by the vertical wind variability in convection combined with the volume mismatch due to the different beamwidths.

Because of the larger beamwidth of the X-SACR, the comparison of spectral widths is less relevant since they can be differently affected by turbulence or wind variability. Nevertheless, reasonably good results are obtained (Figure 14(c)) with significant scatter but practically no bias (correlation, bias and standard deviation of 0.8, −0.02 and 0.15 m s^{-1}, respectively), again confirming good performance of the retrieval of $N_{\text{shape}}(D)$ and of air broadening.

6. Absolute calibration of radar reflectivity

A classic way for absolutely calibrating rainfall radars is to compare the non-attenuated reflectivity computed from the DSD observations of a collocated disdrometer, which provides a 'calibration adjustment' (Williams *et al.*, 2005; Tridon *et al.*, 2013b). However such a procedure is highly uncertain because of the large difference in the sampling size of the instruments, their very different time resolution, and the volume mismatch. In particular, for very light rainfall, the lowest reliable radar measurements at approximately 280 m implies a time delay of several minutes for the rain to reach the ground. Combined with possible evaporation and advection, this calibration methodology must be applied cautiously. Furthermore, for cloud radars, the attenuation due to antenna or radome wetness during precipitation is an additional effect and cannot be easily distinguished from miscalibration (Hogan *et al.*, 2003).

Nevertheless, assuming that ARM radars are absolutely calibrated,* this procedure has been used in the OE2 step of the retrieval as a first-guess estimate of the calibration adjustments C_{Ka} and C_{W}. The rain rate measured by the disdrometer is assumed to be constant up to the first radar range gate, and is used to compute the associated rain attenuation and theoretical attenuated K_a- and W-band reflectivity at $r_{\min} = 280$ m. A time shift depending on the measured K_a-band Doppler velocity $T_{\text{shift}} = r_{\min}/V_{d,K_a}$ is used to correct for the time required by the drops at $r_{\min}$ to reach the disdrometer. Then, sensible estimates of the K_a- and W-band radome attenuation can be derived (blue lines in Figures 15(a) and (b), respectively). It quickly increases after the onset of precipitation (yellow line in Figure 15(a)), and slowly decreases when the rain decays. In this procedure, the radome attenuation is forced to be positive during the non-rainy

*If the radars are not well calibrated, the radome attenuation estimates may also include a miscalibration component which can be considered constant over the whole event.

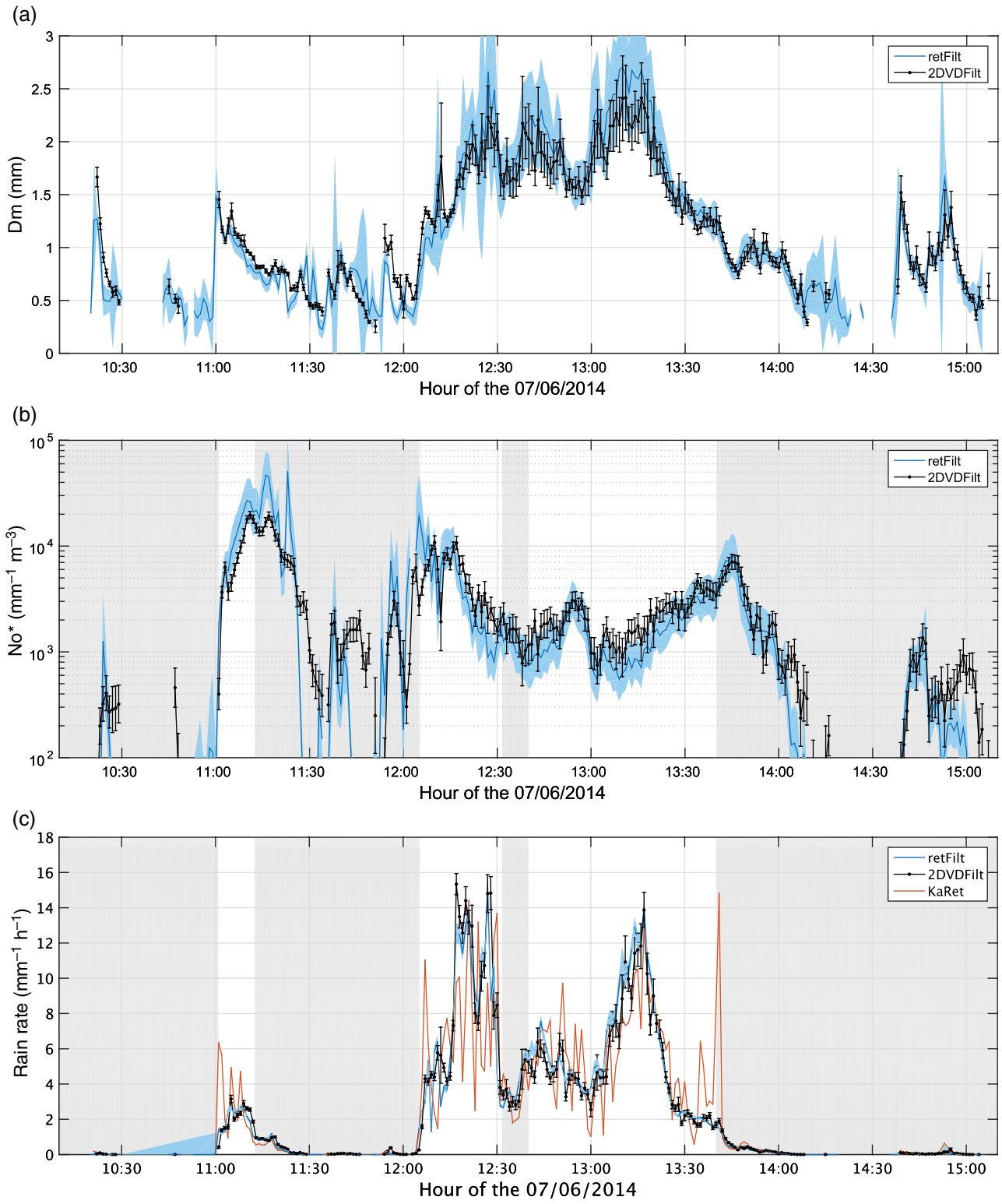

Figure 12. Comparison of retrieved (a) D_m, (b) N_0^* and (c) R (blue line and shading), and those observed by the 2DVD (black errorbars). In (b), the absence of grey shading (ΔA larger than 4 dB) highlights the periods where the retrieval is fully independent of the disdrometer measurements. [Colour figure can be viewed at wileyonlinelibrary.com].

periods. A saturation of the radome attenuation ($\approx$17 and $\approx$5 dB for K_a- and W-band radars, respectively) is reached for moderate rain rate ($R > 2$ mm h^{-1}), which seems to indicate the maximum amount of water that can be held on the radome. A radome attenuation larger at K_a- than at W-band can be explained by their different physical characteristics, e.g. their shape and size (1.81 and 0.61 m, respectively).

The retrieval framework described in section 3.2 provides estimates of the calibration adjustments C_{Ka} and C_W as well. Similarly, the radome attenuation (red lines in Figure 15(a)) can be derived by subtracting the rain attenuation, assuming that the rain rate retrieved at the first radar range gate is constant down to the ground. When the K_a–W differential attenuation is smaller than 4 dB (grey shading), the retrieval is forced to stay close to the first-guess 2DVD estimates. The fact that the retrieval is able to converge using such constraint suggests that these estimates are reasonable. Furthermore, the slightly negative values obtained for the W-band radome attenuation during the non-rainy periods seem to indicate that it was actually miscalibrated by approximately 1 dB. In the presence of moderate precipitation (outside of the grey shading), the significant differential attenuation can be used to absolutely calibrate the

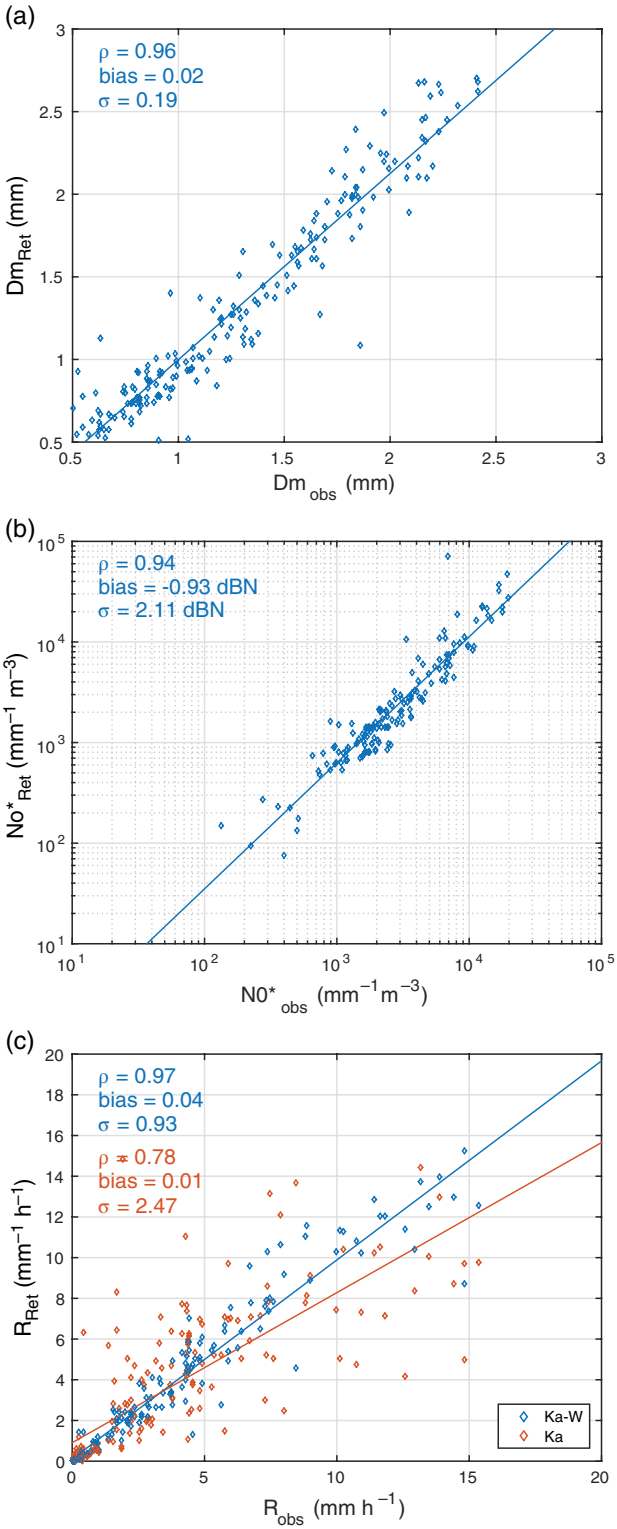

Figure 13. Scatterplots of retrieved versus 2DVD-observed (a) D_m, (b) N_0^* and (c) R. (c) also shows the results of the technique proposed by Chandra *et al.* (2015) using the KAZR only (in orange). [Colour figure can be viewed at wileyonlinelibrary.com].

reflectivities of both radars, independently of the 2DVD estimates. For these periods, the optimal estimation output suggests an accuracy of about 1 dB. This level of accuracy is confirmed by the good agreement with the 2DVD first-order estimation, which is expected to be especially robust in the stratiform period between 1230 and 1330 UTC. However, the retrieval estimation is believed to outperform the 2DVD estimation since it does not involve the combination of data from instruments with very different sampling volumes. Therefore, in the presence of moderate rain, the proposed methodology is believed to provide a robust absolute calibration of radar reflectivities. Such absolutely calibrated reflectivites can then be further used, e.g. to characterize the ice phase above the melting layer.

7. Conclusion

A recently proposed retrieval technique has been improved for its application to a typical midlatitude rain event that occurred in Finland on 7 June 2014, during the the Biogenic Aerosols Effects on Clouds and Climate (BAECC) field campaign. It combines the Doppler spectra profiles observed by two collocated vertically pointing K_a- and W-band radars, and retrieves simultaneously the binned raindrop size distributions (DSD) and different air state parameters, like vertical wind and air broadening. This technique has a high level of complexity with two successive optimal estimation schemes, is designed for high-resolution observations requiring large storage capacity, and is computationally intensive. In this study, it was first applied on a single case-study in order to emphasize its full potential.

The technique provides accurate profiling of the microphysical properties of light to moderate rain ($0.1 < R < 20\,\mathrm{mm\,h^{-1}}$) and explicitly retrieves the calibration constants of the two radars. It has been thoroughly validated by comparisons against DSD observations at the ground from a disdrometer, and independent profile observations of a third collocated Doppler radar operated at X-band. Two domains of applicability have been identified:

1. In light rain ($0.1 < R < 1\,\mathrm{mm\,h^{-1}}$), the retrieval requires the observations of a collocated disdrometer for the calibration of radar reflectivities, generally introducing random errors due to sampling mismatch (volume, position and temporal resolution) between the two instruments. Below $0.1\,\mathrm{mm\,h^{-1}}$, only small and slow-falling drops are present, advection and evaporation of these drops become important and the corresponding errors are too large to provide accurate estimates of the concentration parameter of the DSD.
2. For moderate rain ($R > 1\,\mathrm{mm\,h^{-1}}$), the retrieval is in its optimal range of applicability due to the differential attenuation between the two radar signals which becomes large enough to absolutely calibrate the reflectivity of both radars, and hence provide an estimate of the attenuation due to the antenna or radome wetness. For rain rates larger than approximately $20\,\mathrm{mm\,h^{-1}}$, the retrieval cannot be applied because the strong attenuation of the W-band radar signal leads to its full extinction already at low levels.

The analysed rain event includes a wide range of precipitation type and dynamics conditions (showers, stratiform and convection), and a wide range of processes like evaporation or drop sorting which can lead to very peculiar DSD shapes. It is therefore fairly representative of the capability of the retrieval for precipitation in the midlatitudes.

In a detailed comparison with ground-based observations of the DSD, some discrepancies are found at very small and very large drop diameters, without a clear assessment of which method provides the best estimate. However, such comparison is subject to large uncertainties due to sampling mismatch between the instruments, and these results must be taken with caution. Nevertheless, the central parts of the DSDs, which contribute the most to the main rain parameters, are in very good agreement: for this specific case-study, rain rate, mean volume diameter, and concentration parameter are retrieved with low bias and standard deviations of only $1\,\mathrm{mm\,h^{-1}}$, 0.2 mm and 2 dBN. Furthermore, the non-Rayleigh features necessary for the retrieval are always valuable, i.e. they are neither smoothed by excessive broadening nor undetectable due to too narrow DSDs. Future work will aim at confirming these performances on an extended dataset such as the 180 h of rain of the BAECC campaign.

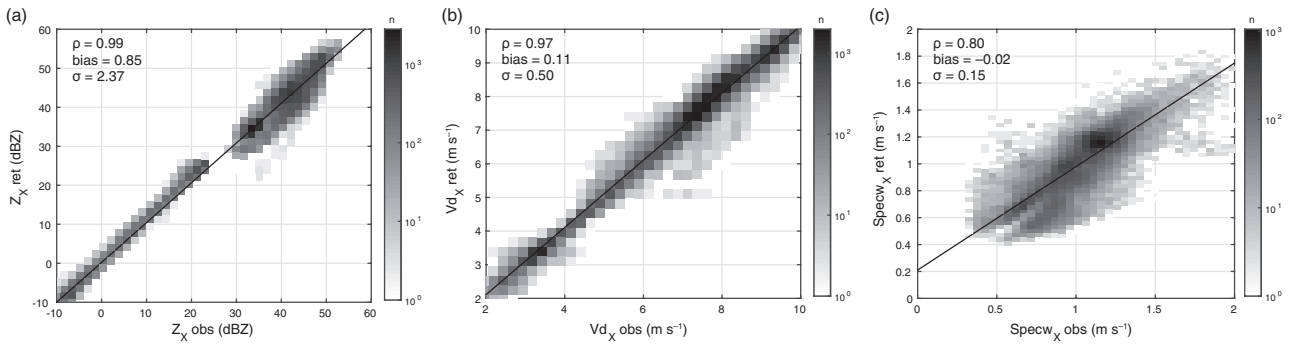

Figure 14. Scatterplots of the first three Doppler moments at X-band (a) reflectivity, (b) Doppler velocity and (c) spectral width, forward modelled from the retrievals as a function of observations by MWCAR. The greyscale indicates the number of points in each bin.

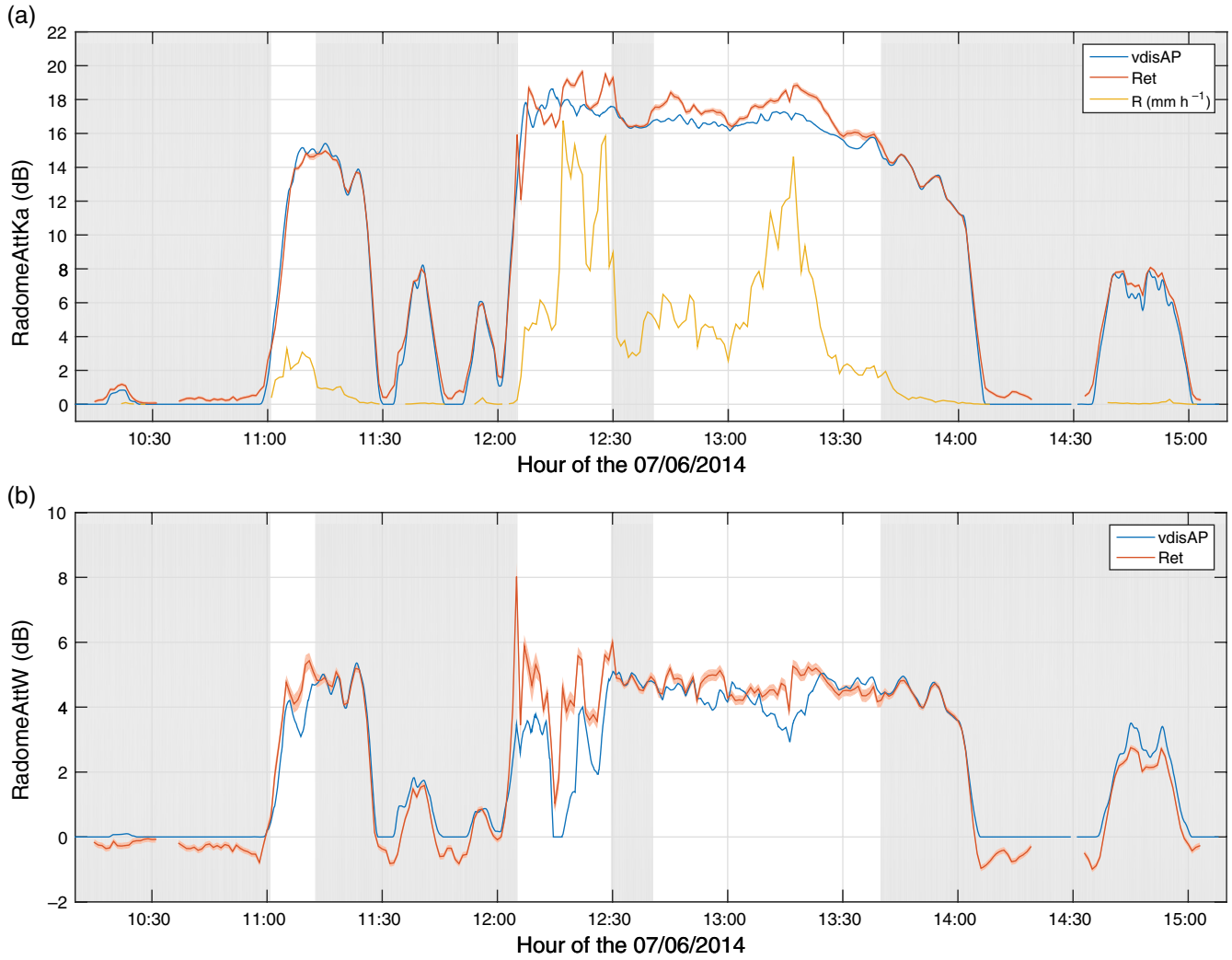

Figure 15. Estimation of the attenuation produced by the radome of the (a) K_a-band and (b) W-band radars as a function of time. The blue line is the preliminary calibration adjustment using the disdrometer whilst the red line denotes to the retrieval estimate. For reference, absence of grey shading (ΔA larger than 4 dB) highlights the periods where the retrieval is fully independent of the disdrometer measurements, and the corresponding rain rate is indicated by the yellow line. [Colour figure can be viewed at wileyonlinelibrary.com].

The retrieval provides the DSD variability at a very high resolution (30 m in vertical, every 2 s) corresponding to the cloud radar data high resolution which is necessary to keep small the air broadening of Doppler spectra. Such resolution is probably too high for direct comparisons with models or satellite observations, but it can be easily up-scaled to match their resolution.

Applied to increasingly common multi-frequency Doppler radar observations, the statistics of the DSD and its vertical variability derived from this retrieval will provide valuable information for a variety of applications. First, the characterization of spatio-temporal variability of the retrieved DSD and its moments can help in refining satellite rainfall retrievals (e.g. Global Precipitation Measurement mission retrievals; Hou *et al.*, 2014). For example, what is the vertical variability of rain parameters within a GPM pixel? Which shape parameter is the best to represent a parametrized DSD? Does it change with the distance from the melting layer and cloud base? Second, in combination with polarimetric observations from scanning radars, the fine description of the vertical variability of precipitation will improve our understanding of the vertical profile of polarimetric variables (Kumjian and Prat, 2014) and lead to better quantitative precipitation estimations from scanning radars, e.g. by better accounting for evaporation. Finally, some features derived for

this case-study pinpoint signatures of microphysical processes such as evaporation or drop sorting. Future work on the vertical variability of the DSD will aim at fingerprinting and improving our understanding of these processes active in the warm segment of the profile. For example, following Prat *et al.* (2008), the vertical variability of the DSD can be used to evaluate the collision–coalescence schemes in bin models. These schemes have been determined from extensive modelling and laboratory studies, but have rarely been compared to real observations in nature. Finally, such observations are critically needed for the validation of two-moment parametrizations and can ultimately lead to numerical weather prediction model improvement.

Acknowledgements

This work was funded by the project 'Calibration and validation studies over the North Atlantic and UK for the Global Precipitation Mission' funded by the UK NERC (NE/L007169/1). This research used the SPECTRE and ALICE High Performance Computing Facilities at the University of Leicester. The authors thank Dr D'Adderio for useful discussions and three anonymous reviewers for their helpful comments which improved the manuscript.

References

Atlas D, Srivastava RC, Sekhon RS. 1973. Doppler radar characteristics of precipitation at vertical incidence. *Rev. Geophys.* **11**: 1–35.

Battaglia A, Westbrook CD, Kneifel S, Kollias P, Humpage N, Löhnert U, Tyynelä J, Petty GW. 2014. G-band (140–220 GHz) atmospheric radars: New frontiers in cloud physics. *Atmos. Meas. Tech.* **7**: 1527–1546.

Beard KV, Chuang C. 1987. A new model for the equilibrium shape of raindrops. *J. Atmos. Sci.* **44**: 1509–1524.

Borque P, Luke E, Kollias P. 2016. On the unified estimation of turbulence eddy dissipation rate using Doppler cloud radars and lidars. *J. Geophys. Res.* **120**: 5972–5989. https://doi.org/10.1002/2015JD024543.

Bringi VN, Williams CR, Thurai M, May PT. 2009. Using dual-polarized radar and dual-frequency profiler for DSD characterization: A case study from Darwin, Australia. *J. Atmos. Oceanic Technol.* **26**: 2107–2122.

Chandra A, Zhang C, Kollias P, Matrosov S, Szyrmer W. 2015. Automated rain rate estimates using the Ka-b and ARM zenith radar (KAZR). *Atmos. Meas. Tech.* **8**: 3685–3699.

Cifelli R, Williams CR, Rajopadhyaya DK, Avery SK, Gage KS, May PT. 2000. Drop-size distribution characteristics in tropical mesoscale convective systems. *J. Appl. Meteorol.* **39**: 760–777.

Gage KS, Williams CR, Clark WL, Johnston PE, Carter DA. 2002. Profiler contributions to tropical rainfall measuring mission (TRMM) ground validation field campaigns. *J. Atmos. Oceanic Technol.* **19**: 843–863.

Giangrande SE, Luke EP, Kollias P. 2010. Automated retrievals of precipitation parameters using non-Rayleigh scattering at 95 GHz. *J. Atmos. Oceanic Technol.* **27**: 1490–1503.

Giangrande SE, Luke EP, Kollias P. 2012. Characterization of vertical velocity and drop size distribution parameters in widespread precipitation at ARM facilities. *J. Appl. Meteorol. Climatol.* **51**: 380–391.

Hogan RJ, Bouniol D, Ladd DN, O'Connor EJ, Illingworth AJ. 2003. Absolute calibration of 94/95 GHz radars using rain. *J. Atmos. Oceanic Technol.* **20**: 572–580.

Hogan RJ, Gaussiat N, Illingworth AJ. 2005. Stratocumulus liquid water content from dual-wavelength radar. *J. Atmos. Oceanic Technol.* **22**: 1207–1218.

Hou AY, Kakar RK, Neeck S, Azarbarzin AA, Kummerow CD, Kojima M, Oki R, Nakamura K, Iguchi T. 2014. The global precipitation measurement mission. *Bull. Am. Meteorol. Soc.* **95**: 701–722.

Kneifel S, Kollias P, Battaglia A, Leinonen J, Maahn M, Kalesse H, Tridon F. 2016. First observations of triple-frequency radar Doppler spectra in snowfall: Interpretation and applications. Geophys. Res. Lett. **43**: 2225–2233. https://doi.org/10.1002/2015GL067618.

Kollias P, Albrecht B, Marks F. 2002. Why Mie? Accurate observations of vertical air velocities and raindrops using a cloud radar. *Bull. Am. Meteorol. Soc.* **83**: 1471–1483.

Kruger A, Krajewski WF. 2002. Two-dimensional video disdrometer: A description. *J. Atmos. Oceanic Technol.* **19**: 602–617.

Kumjian M, Ryzhkov A. 2010. The impact of evaporation on polarimetric characteristics of rain: Theoretical model and practical implications. *J. Appl. Meteor. Climatol.* **49**: 1247–1267.

Kumjian MR, Prat OP. 2014. The impact of raindrop collisional processes on the polarimetric radar variables. *J. Atmos. Sci.* **71**: 3052–3067.

Leinonen J, Moisseev D, Leskinen M, Petersen WA. 2012. A climatology of disdrometer measurements of rainfall in Finland over five years with implications for global radar observations. *J. Appl. Meteorol. Climatol.* **51**: 392–404.

Lhermitte R. 1990. Attenuation and scattering of millimeter wavelength radiation by clouds and precipitation. *J. Atmos. Oceanic Technol.* **7**: 464–479.

Li X, Srivastava RC. 2001. An analytical solution for raindrop evaporation and its application to radar rainfall measurements. *J. Appl. Meteorol.* **40**: 1607–1616.

Lin X, Hou AY. 2012. Estimation of rain intensity spectra over the continental United States using ground radar-gauge measurements. *J. Clim.* **25**: 1901–1915.

McFarquhar MG. 2004. The effect of raindrop clustering on collision-induced break-up of raindrops. *Q. J. R. Meteorol. Soc.* **130**: 2169–2190.

Mather JH, Voyles JW. 2013. The ARM climate research facility: A review of structure and capabilities. *Bull. Am. Meteorol. Soc.* **94**: 377–392.

Matrosov SY. 2005. Attenuation-based estimates of rainfall rates aloft with vertically pointing Ka-band radars. *J. Atmos. Oceanic Technol.* **22**: 43–54.

Matrosov SY. 2017. Characteristic raindrop size retrievals from measurements of differences in vertical Doppler velocities at Ka- and W-band radar frequencies *J. Atmos. Oceanic Technol.* **34**: 65–71. https://doi.org/10.1175/JTECH-D-16-0181.1.

Meneghini R, Kim H, Liao L, Jones JA, Kwiatkowski JM. 2015. An initial assessment of the surface reference technique applied to data from the dual-frequency precipitation radar (DPR) on the GPM satellite. *J. Atmos. Oceanic Technol.* **32**: 2281–2296.

Morrison H, Milbrandt J. 2011. Comparison of two-moment bulk microphysics schemes in idealized supercell thunderstorm simulations. *Mon. Weather Rev.* **139**: 1103–1130.

Morrison H, Tessendorf SA, Ikeda K, Thompson G. 2012. Sensitivity of a simulated midlatitude squall line to parameterization of raindrop breakup. *Mon. Weather Rev.* **140**: 2437–2460.

Mugnai A, Michele SD, Smith EA, Baordo F, Bauer P, Bizzarri B, Joe P, Kidd C, Marzano FS, Tassa A, Testud J, Tripoli GJ. 2005. Snowfall measurements by the proposed European GPM Mission. In *Measuring Precipitation from Space: EURAINSAT and the Future*, Chapter 49, Levizzani V, Bauer P, Turk JF. (eds.): 655–674. Springer: Dordrecht, The Netherlands.

Petäjä T, O'Connor EJ, Moisseev D, Sinclair VA, Manninen AJ, Väänänen R, von Lerber A, Thornton JA, Nicoll K, Petersen W, Chandrasekar V, Smith JN, Winkler PM, Krüger O, Hakola H, Timonen H, Brus D, Laurila T, Asmi E, Riekkola ML, Mona L, Massoli P, Engelmann R, Komppula M, Wang J, Kuang C, Bäck J, Virtanen A, Levula J, Ritsche M, Hickmon N. 2016. BAECC: A field campaign to elucidate the impact of Biogenic Aerosols on Clouds and Climate. *Bull. Am. Meteorol. Soc.* **97**: 1909–1928.

Peters G, Fischer B, Münster H, Clemens M, Wagner A. 2005. Profiles of raindrop size distributions as retrieved by microrain radars. *J. Appl. Meteorol. Climatol.* **44**: 1930–1949.

Peters G, Fischer B, Clemens M. 2010. Rain attenuation of radar echoes considering finite-range resolution and using drop size distributions. *J. Atmos. Oceanic Technol.* **27**: 829–842.

Pounder NL, Hogan RJ, Várnai T, Battaglia A, Cahalan RF. 2012. A variational method to retrieve the extinction profile in liquid clouds using multiple-field-of-view lidar. *J. Appl. Meteorol. Climatol.* **51**: 350–365.

Prat OP, Barros AP, Williams CR. 2008. An intercomparison of model simulations and VPR estimates of the vertical structure of warm stratiform rainfall during TWP-ICE. *J. Appl. Meteorol. Climatol.* **47**: 2797–2815.

Rodgers CD. 2000. *Inverse Methods for Atmospheric Sounding: Theory and Practice*, World Scientific: Singapore.

Rosenkranz PW. 1998. Water vapor microwave continuum absorption: A comparison of measurements and models. *Radio Sci.* **33**: 919–928.

Schafer R, Avery S, May P, Rajopadhyaya D, Williams C. 2002. Estimation of rainfall drop size distributions from dual-frequency wind profiler spectra using deconvolution and a nonlinear least-squares fitting technique. *J. Atmos. Oceanic Technol.* **19**: 864–874.

Testud J, Oury S, Black RA, Amayenc P, Dou X. 2001. The concept of 'normalized' distribution to describe raindrop spectra: A tool for cloud physics and cloud remote sensing. *J. Appl. Meteorol. Climatol.* **40**: 1118–1140.

Thurai M, Williams CR, Bringi VN. 2014. Examining the correlations between drop size distribution parameters using data from two side-by-side 2D-video disdrometers. *Atmos. Res.* **144**: 95–110.

Tokay A, Petersen WA, Gatlin P, Wingo M. 2013. Comparison of raindrop size distribution measurements by collocated disdrometers. *J. Atmos. Oceanic Technol.* **30**: 1672–1690.

Tridon F, Battaglia A. 2015. Dual-frequency radar Doppler spectral retrieval of rain drop size distributions and entangled dynamics variables. *J. Geophys. Res.* **120**: 5585–5601. https://doi.org/10.1002/2014JD023023.

Tridon F, Battaglia A, Kollias P. 2013a. Disentangling Mie and attenuation effects in rain using a Ka–W dual-wavelength Doppler spectral ratio technique. *Geophys. Res. Lett.* **40**: 5548–5552. https://doi.org/10.1002/2013GL057454.

Tridon F, Battaglia A, Kollias P, Luke E, Williams CR. 2013b. Signal postprocessing and reflectivity calibration of the atmospheric radiation measurement program 915-MHz wind profilers. *J. Atmos. Oceanic Technol.* **26**: 1120–1134.

Williams CR. 2016. Reflectivity and liquid water content vertical decomposition diagrams to diagnose vertical evolution of raindrop size distributions. *J. Atmos. Oceanic Technol.* **33**: 579–595.

Williams CR, Gage KS, Clark W, Kucera P. 2005. Monitoring the reflectivity calibration of a scanning radar using a profiling radar and a disdrometer. *J. Atmos. Oceanic Technol.* **22**: 1004–1018.

Wilson DR, Illingworth AJ, Blackman TM. 1997. Differential Doppler velocity: A radar parameter for characterizing hydrometeor size distributions. *J. Appl. Meteorol.* **36**: 649–663.